The Astrophysical Journal, 792:1 (17pp), 2014 September 1 doi:10.1088/0004-637X/792/1/1

UNDERSTANDING THE MASS–RADIUS RELATION FOR SUB-NEPTUNES: RADIUS AS A PROXY FOR COMPOSITION

Eric D. Lopez and Jonathan J. Fortney
Department of Astronomy and Astrophysics, University of California, Santa Cruz, CA 95064, USA
Received 2013 November 1; accepted 2014 June 13; published 2014 August 7

ABSTRACT

Transiting planet surveys like *Kepler* have provided a wealth of information on the distribution of planetary radii, particularly for the new populations of super-Earth- and sub-Neptune-sized planets. In order to aid in the physical interpretation of these radii, we compute model radii for low-mass rocky planets with hydrogen–helium envelopes. We provide model radii for planets 1–20 $M_\oplus$, with envelope fractions 0.01%–20%, levels of irradiation 0.1–1000 times Earth's, and ages from 100 Myr to 10 Gyr. In addition we provide simple analytic fits that summarize how radius depends on each of these parameters. Most importantly, we show that at fixed H/He envelope fraction, radii show little dependence on mass for planets with more than ∼1% of their mass in their envelope. Consequently, planetary radius is to a first order a proxy for planetary composition, i.e., H/He envelope fraction, for Neptune- and sub-Neptune-sized planets. We recast the observed mass–radius relationship as a mass–*composition* relationship and discuss it in light of traditional core accretion theory. We discuss the transition from rocky super-Earths to sub-Neptune planets with large volatile envelopes. We suggest ∼1.75 $R_\oplus$ as a physically motivated dividing line between these two populations of planets. Finally, we discuss these results in light of the observed radius occurrence distribution found by *Kepler*.

Key words: planets and satellites: composition – planets and satellites: formation – planets and satellites: interiors – planets and satellites: physical evolution

Online-only material: color figures

1. INTRODUCTION

NASA's *Kepler* mission has been an enormous success, discovering over 3500 planet candidates to date (Borucki et al. 2011; Batalha et al. 2013). Among the mission's many firsts and accomplishments, however, one of the most revolutionary is that for the first time we have a robust determination of the relative abundance of different sizes of planets, stretching from Earth-sized all the way up to the largest hot Jupiters (Howard et al. 2012; Fressin et al. 2013; Petigura et al. 2013b).

In particular, *Kepler* has discovered an abundant new population of ∼3 $R_\oplus$ planets (Fressin et al. 2013; Petigura et al. 2013b). Although smaller than Neptune, these planets are large enough that they must have substantial hydrogen and helium (hereafter H/He) envelopes to explain their radii. Such planets are unlike anything found in our own solar system, and fundamental questions about their structure and formation are still not understood. Are these Neptune-like planets that form beyond the snow line and contain large amounts of volatile ices (Rogers et al. 2011), or are these scaled-up terrestrial worlds with H/He envelopes that formed close to their current orbits (Hansen & Murray 2013; Chiang & Laughlin 2013)?

In an attempt to address these questions, a great deal of effort has been invested in acquiring precise masses for a large number of these transiting planets. In recent years this has generated a much fuller understanding of the mass–radius relation, especially for sub-Neptune- and super-Earth-sized planets (Weiss et al. 2013). In particular, there are now several multiplanet *Kepler* systems like Kepler-11 with masses determined from transit timing variations (TTVs; e.g., Lissauer et al. 2011, 2013; Carter et al. 2012; Cochran et al. 2011). Although rare, such systems are incredibly valuable because with both a mass and a radius we can estimate a planet's bulk composition using models of interior structure and thermal evolution (e.g., Rogers & Seager 2010a; Nettelmann et al. 2011; Miller & Fortney 2011; Lopez et al. 2012; Valencia et al. 2013). Thus far, efforts have been focused on individually determining compositions for this handful of planets. This paucity stands in stark contrast to the over 3500 *Kepler* candidates with only measured radii. Unfortunately, the vast majority of these candidates are in dynamically inactive systems without strong TTVs or around distant stars too faint for radial velocity measurements.

Moreover, even with precise masses and radii there are inherent degeneracies that limit ones ability to constrain the bulk compositions of super-Earth-sized planets. For 1–2 $R_\oplus$ planets, the densities of water, silicate rocks, and iron (i.e., ∼1–10 g cm^{-3}) are similar enough that it is impossible to uniquely constrain the relative abundance of these components (Valencia et al. 2007; Rogers & Seager 2010a). To some extent, models of planet collisions can set upper limits on the maximum iron or water mass fractions that are physically achievable (Marcus et al. 2009, 2010), but for a given planet this still allows for a wide range of internal compositions.

Fortunately, models are still able to set clear and useful constraints on composition. In particular, thermal evolution models can set robust constraints on the fraction of a planet's mass in an H/He envelope. Due to its significantly lower density, even a relatively minor amount of H/He (e.g., ∼1% of total planet mass) has a large impact on planetary radius. For sub-Neptune-sized ∼3 $R_\oplus$ or larger planets, the H/He envelope will dominate a planet's size regardless of the abundance of other elements. As a result, for these planets, any degeneracies between rock, water, and iron are secondary to the overall distribution of material between the H/He envelope and heavier elements.

Moreover, for sub-Neptune-sized planets at fixed bulk composition, theoretical mass–radius curves are remarkably flat; that is, planets with a given H/He abundance have very similar

sizes regardless of their mass (Lopez et al. 2012). As a result, there is a remarkably tight relationship between planetary radius and H/He envelope fraction that is independent of planet mass. Critically, this opens up the hope of constraining H/He envelope fractions for the vast population of Neptune- and sub-Neptune-sized *Kepler* candidates without measured masses. This is what we begin to explore in this paper.

Whenever possible it is still preferable to obtain a well-measured mass. Planet mass is critical for understanding how volatile-rich planets accrete their initial H/He envelope (Bodenheimer et al. 2000; Ikoma & Hori 2012) and whether they can retain it against X-ray- and EUV-driven photoevaporation (Lopez et al. 2012; Lopez & Fortney 2013; Owen & Jackson 2012; Owen & Wu 2013). Nevertheless, for systems of sub-Neptunes like Kepler-11, even a factor of ∼two uncertainties in planet masses are sufficient to tightly constrain H/He envelope fractions with precise radii (Lissauer et al. 2013). This fact means that instead of only examining the *radius* distribution of *Kepler* candidates, we can begin thinking about a *composition* distribution.

2. MODELS

In order to understand how planetary radius relates to planet mass and envelope fraction, it is necessary to fully model how a planet cools and contracts due to thermal evolution. For this work, we have used the thermal evolution presented in Lopez et al. (2012), where additional model details can be found. Similar models are frequently used to track the evolution of sub-Neptunes and hot Jupiters (e.g, Miller & Fortney 2011; Nettelmann et al. 2011). Unlike Lopez et al. (2012) and Lopez & Fortney (2013), here we do not consider the effects of photoevaporation. Although photoevaporation can have a large impact on the H/He envelope fraction of a planet (e.g., Baraffe et al. 2006; Hubbard et al. 2007; Lopez et al. 2012; Owen & Jackson 2012), the effect on the thermal state of the interior is relatively minor (Lopez & Fortney 2013). Here we are primarily interested in the relationship between radius and H/He envelope fraction as controlled by thermal evolution; as a result, the effects of photoevaporation can be ignored. In essence, the present-day envelope fraction determines the radius, but that envelope fraction may have been strongly affected by formation and photoevaporation.

At a given age, a model is defined by the mass of its heavy-element core, the mass of its H/He envelope, the amount of incident radiation it receives, and the internal specific entropy of its H/He envelope. As a default model, we assume an isothermal rock/iron core with an Earth-like 2:1 rock/iron ratio, using the ANEOS olivine (Thompson 1990) and SESAME 2140 Fe (Lyon & Johnson 1992) equations of state (EOS). When determining envelope fraction error bars for observed planets, however, we varied this iron fraction from pure rock to the maximum possible iron fraction from impact models in Marcus et al. (2010). For the H/He envelope we assume a fully adiabatic interior using the Saumon et al. (1995) EOS. In addition we consider the possibility of water worlds and three-component models using the H2O-REOS for water (Nettelmann et al. 2008). Finally, atop the H/He envelope is a relatively small radiative atmosphere, which we assume is isothermal at the equilibrium temperature. We define a planet's radius at 20 mbar, appropriate for the slant viewing geometry in optical transits for solar metallicity, although our results are insensitive to the exact pressure level chosen (Hubbard et al. 2001).

In order to quantitatively evaluate the cooling and contraction of the H/He envelope, we use a model atmosphere grid over a range of surface gravities and incident fluxes. These grids relate the surface gravity and internal specific entropy to the intrinsic temperature of the flux emitted for a given model. The intrinsic temperature $T_{\rm int} = (T_{\rm eff}^4 - T_{\rm eq}^4)^{1/4}$ is the equivalent blackbody temperature of the net radiation leaving a planet; it is approximately the temperature the planet would have if the parent star were removed. These one-dimensional radiative–convective models are computed for solar metallicity and for 50 times solar metallicity enhanced-opacity atmospheres using the methods described in Fortney et al. (2007) and Nettelmann et al. (2011). These atmosphere models are fully nongray; that is, wavelength-dependent radiative transfer is performed rather than simply assuming a single infrared opacity. The atmospheres of Neptune- and sub-Neptune-sized planets might be significantly enhanced in metals (Fortney et al. 2013) or host extended clouds that greatly enhance atmospheric opacity (Morley et al. 2013). Therefore, our two atmosphere grids are a way to make a simplified first estimate of the role of enhanced opacity on planetary thermal evolution. For all runs we use the H/He Saumon et al. (1995) EOS for the envelope.

At very early times and very low masses, the models reach gravities beyond the edge of our cooling grid. In such cases we logarithmically extrapolate the intrinsic temperature $T_{\rm int}$ as a function of gravity. This does not significantly affect our results, however, because the dependence of $T_{\rm int}$ on gravity is slight and the models are only at such low gravities in the first few megayears.

Finally, we include heating from radioactive decay in the rock/iron core and the delay in cooling due to the core's heat capacity. In order to correctly determine the mass–radius envelope fraction relationship, it is vital to include these thermal evolution effects because these will significantly delay cooling and contraction, particularly for planets less than ∼5 $M_\oplus$ (Lopez et al. 2012)

$$\int_{M_{\rm core}}^{M_{\rm p}} dm \frac{T\,dS}{dt} = -L_{\rm int} + L_{\rm radio} - c_{\rm v} M_{\rm core} \frac{dT_{\rm core}}{dt}. \quad (1)$$

Equation (1) (Nettelmann et al. 2011; Lopez et al. 2012) summarizes our thermal evolution models. The left-hand side describes the cooling rate of the H/He envelope. Positive terms on the right-hand side represent energy sources that heat and inflate a planet, while negative terms represent energy losses that allow a planet to cool and contract. The term $L_{\rm int} = 4\pi R_{\rm p}^2 \sigma T_{\rm int}^4$ accounts for cooling from the atmospheric radiative transfer models described above. The term $L_{\rm radio}$ describes radioactive heating, with abundances given by Anders & Grevesse (1989). Finally, $dT_{\rm core}/dt$ represents the cooling of the rocky core. For gas-rich planets with large H/He adiabats, the surface of the rocky core is at large pressures of many kilobars and high temperatures, typically >2000 K. Under these circumstances, the rocky surface will be partially or completely molten, and heat can be transferred easily between the rocky core and the gaseous envelope Henning et al. (2009). Therefore, temperature will be continuous across the core–envelope boundary. As the gaseous envelope cools due to radiation through the atmosphere, so too will the rocky core. For sub-Neptunes with most of their mass in the rocky core, the core is the dominant energy reservoir. Therefore, including this term lengthens a planet's cooling timescale and slows its contraction as discussed. We assume a core heat capacity of $c_v = 0.5$–1.0 J K^{-1} g^{-1} as appropriate for high-pressure silicates (Alfè et al. 2002; Guillot et al. 1995;

Valencia et al. 2010). Each of these terms is described in detail in Nettelmann et al. (2011) and Lopez et al. (2012).

As with previous models, we assume that planets initially form with a large initial entropy according to the traditional hot-start model (Fortney et al. 2007; Marley et al. 2007). Specifically, we start our models at an age of 1 Myr with a large initial entropy of 10 k_b baryon^{-1}. This assumption does not significantly affect any of our results because hot-start and cold-start models are indistinguishable by the time planets are ∼100 Myr old (Marley et al. 2007; Lopez et al. 2012). Moreover, Mordasini (2013) recently showed that for planets less massive than Jupiter gravitational heating due to settling of heavy elements in the H/He envelope can erase any difference between hot and cold starts.

For low-mass planets, the hot-start assumption results in extremely large initial radii, $\gtrsim$10 $R_\oplus$. However, as we explore in Section 3.2, such models cool extremely rapidly such that significant contraction has already occurred by several megayears. In general we present results at ages >10 Myr, when our results are insensitive to the initial choice of entropy.

3. A MASS–RADIUS PARAMETER STUDY

Planetary radius is an invaluable tool in understanding the nature of low-mass planets; however, without the aid of thermal evolution models like those used here, it can be quite difficult to interpret. In order to better understand the information contained in planet radii, we performed a detailed parameter study of our thermal evolution and structure models for sub-Neptune-type planets with rock/iron cores and thick H/He envelopes.

As part of this parameter study, we ran over 1300 thermal evolution models, varying planet mass, incident flux, envelope fraction, and atmospheric metallicity. We covered planets from 1 to 20 $M_\oplus$, 0.1–1000 $F_\oplus$, and 0.01%–60% H/He, for both solar metallicity and enhanced-opacity models. We then recorded planet radius at every age from 10 Myr to 10 Gyr. The results of this study are summarizedin Figure 1 and Tables 1–6.

Examining Figure 1, it is immediately clear that isocomposition mass–radius curves are in fact remarkably flat for sub-Neptune or larger planets, at least once they are a few gigayears old. In each panel, we show theoretical mass–radius curves while varying the H/He envelope fraction, incident flux, and age of the model planets. For the parameters that are not varying in each panel, we use representative values of 5% H/He, 100 $F_\oplus$, and 5 Gyr.

Turning to panel (a), we see the enormous effect that varying the H/He envelope fraction has on planetary radius. By comparison, any other changes to incident flux, age, or internal structure are secondary. For planets with envelopes ∼0.1% of their total mass, the mass–radius curve does increase slightly from ∼1.5 $R_\oplus$ at 1 $M_\oplus$ to ∼2.5 $R_\oplus$ at 20 $M_\oplus$. For envelopes this insubstantial, a planet's size is still dominated by its rocky/iron core, and so the mass–radius curves have a slope similar to the bare rock curve shown in Figure 1. However, as we increase the envelope fraction, the mass–radius curves rapidly flatten, beginning at low masses, until by ∼3% H/He the curves are almost completely flat.

By comparison, panel (b) in Figure 1 shows the much more modest effect of varying the incident flux. More-irradiated planets tend to be slightly larger because they have a large scale height in their atmospheres and because the irradiation alters the radiative transfer through their atmosphere, slowing their contraction (Fortney et al. 2007). Nonetheless, despite varying the incident flux by four orders of magnitude, planet radii vary by less than ∼30%.

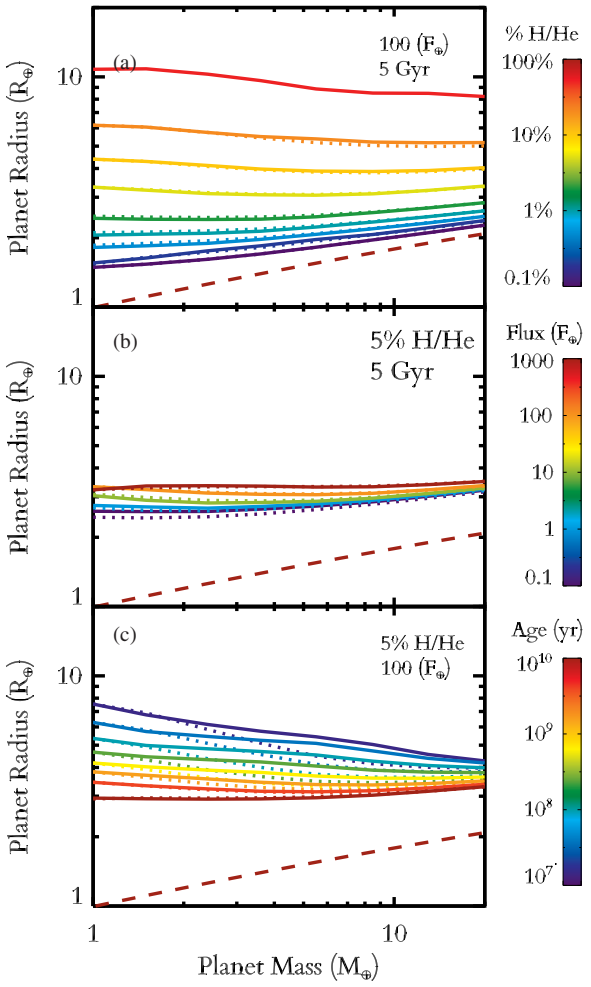

Figure 1. Here we show model mass–radius relations from 1 to 20 $M_\oplus$ and how these depend on H/He envelope fraction, irradiation, and age, indicated by the colors. Solid lines correspond to enhanced-opacity models, while dotted lines correspond to solar metallicity. The dashed rust-colored lines show the size of bare rocky planets with Earth-like rock/iron abundances. Our default model is 5% H/He, 5 Gyr old, and receives ∼100 $F_\oplus$. In panel (a) we vary the H/He envelope fraction from 0.1% to 60% H/He; this has by far the largest impact on planet size. Below ∼3% H/He, radius increases modestly with mass due to the dominance of the rocky core. For larger envelopes, the mass–radius relation is remarkably flat until for gas giant-sized planets it decreases slightly with higher mass due to the increasing self-gravity of the envelope. In panel (b) we vary the incident flux a planet receives from 1 to 1000 $F_\oplus$. Despite varying the irradiation by four orders of magnitude, the radius never changes by more than ∼30%. Finally, in panel (c) we show a time evolution from 10 Myr to 10 Gyr. At early times low-mass planets are larger than higher-mass planets due to their lower gravities. However, these low-mass planets are able to cool more rapidly, which gradually flattens the mass–radius relation.

(A color version of this figure is available in the online journal.)

Finally, panel (c) shows how these mass–radius curves evolve over time. At early times, lower-mass planets are significantly larger than higher-mass planets due to their similarly large internal energies and lower gravities. Over time, however, these low-mass planets are able to cool more rapidly than their more-massive relatives, which gradually flattens the mass–radius curves. By the time the planets are ∼ 1 Gyr old we see the characteristically flat mass–radius curves for H/He-rich planets.

Table 1
Low-mass Planet Radii at 100 Myr, Solar Metallicity

Flux ($F_\oplus$)	Mass ($M_\oplus$)	0.01%	0.02%	0.05%	0.1%	0.2%	0.5%	1%	2%	5%	10%	20%
0.1	1	1.22	1.16	1.18	1.21	1.32	1.65	2.17	2.75	4.32	6.81	11.7
0.1	1.5	1.30	1.24	1.26	1.30	1.40	1.71	2.15	2.65	3.97	6.18	10.6
0.1	2.4	1.41	1.36	1.40	1.42	1.53	1.79	2.17	2.58	3.66	5.36	9.05
0.1	3.6	1.53	1.49	1.51	1.54	1.64	1.89	2.21	2.56	3.49	4.93	7.86
0.1	5.5	1.66	1.63	1.66	1.69	1.79	2.01	2.28	2.60	3.37	4.58	6.96
0.1	8.5	1.81	1.79	1.82	1.85	1.95	2.14	2.39	2.67	3.36	4.35	6.32
0.1	13	1.97	1.97	1.98	2.02	2.11	2.30	2.52	2.78	3.41	4.29	5.94
0.1	20	2.15	2.15	2.17	2.20	2.29	2.47	2.67	2.93	3.52	4.32	5.75
10	1	1.32	1.24	1.27	1.31	1.44	1.82	2.40	3.06	4.72	7.13	11.1
10	1.5	1.36	1.32	1.35	1.38	1.50	1.84	2.32	2.88	4.31	6.47	10.4
10	2.4	1.46	1.43	1.48	1.50	1.59	1.88	2.26	2.71	3.88	5.67	9.14
10	3.6	1.57	1.55	1.58	1.60	1.71	1.95	2.27	2.64	3.61	5.13	8.11
10	5.5	1.69	1.68	1.71	1.73	1.84	2.05	2.33	2.66	3.46	4.70	7.13
10	8.5	1.84	1.83	1.86	1.89	1.98	2.18	2.43	2.72	3.42	4.43	6.39
10	13	1.99	2.01	2.02	2.05	2.14	2.32	2.55	2.82	3.46	4.35	5.96
10	20	2.17	2.18	2.19	2.23	2.31	2.49	2.69	2.95	3.56	4.37	5.77
1000	1	1.59	1.63	1.70	1.75	1.83	2.30	3.12	3.99	6.21	8.88	11.3
1000	1.5	1.63	1.67	1.72	1.77	1.89	2.31	3.02	3.83	6.01	9.41	14.0
1000	2.4	1.70	1.72	1.77	1.81	1.93	2.32	2.90	3.55	5.35	8.59	15.4
1000	3.6	1.77	1.79	1.83	1.87	1.99	2.34	2.81	3.36	4.82	7.27	13.4
1000	5.5	1.87	1.88	1.92	1.96	2.08	2.37	2.76	3.22	4.39	6.25	10.3
1000	8.5	1.99	2.00	2.03	2.08	2.19	2.50	2.76	3.15	4.12	5.56	8.48
1000	13	2.12	2.12	2.15	2.21	2.31	2.58	2.81	3.16	3.99	5.18	7.43
1000	20	2.27	2.27	2.30	2.35	2.45	2.68	2.90	3.21	3.94	4.97	6.80

Notes. Radii of planets, in $R_\oplus$. Column 1 is incident flux on the planet, relative to the solar constant. Column 2 is the total planet mass in $M_\oplus$. Otherwise, column headers indicate the fraction of a planet's mass in the H/He envelope.

3.1. Describing Radius with Power Laws

A quick inspection of Figure 1 makes clear that not all of a planet's properties have an equal impact on planet size. Planet mass and incident flux have only a modest impact on planet size, while planet age has a larger impact, particularly at younger ages. However, by far the largest determinant of a planet's size is the fraction of its mass in an H/He envelope. One way to quantify the relative importance of envelope fraction is to construct analytic fits for radius as a function of planet mass $M_{\rm p}$, H/He envelope fraction $f_{\rm env}$, incident flux $F_\oplus$, and age. In Lopez & Fortney (2013) we performed a similar analysis, examining planets' vulnerability to photoevaporative mass loss.

Fortunately, the relationships between radius and each of these parameters are all reasonably well described by power laws, and the effects of each variable are relatively independent. As a result, we can do a reasonably good job of describing the results of our full parameter study with a set of four independent power laws. The one caveat is that we do not fit for the total planet radius $R_{\rm p}$ but instead the radius of the H/He envelope $R_{\rm env} \approx R_{\rm p} - R_{\rm core}$, where $R_{\rm core}$ is the size of the

Table 2
Low-mass Planet Radii at 1 Gyr, Solar Metallicity

Flux ($F_\oplus$)	Mass ($M_\oplus$)	0.01%	0.02%	0.05%	0.1%	0.2%	0.5%	1%	2%	5%	10%	20%
0.1	1	1.07	1.09	1.12	1.15	1.28	1.55	1.79	2.13	2.98	4.26	6.74
0.1	1.5	1.18	1.19	1.22	1.26	1.38	1.62	1.82	2.13	2.87	3.96	6.10
0.1	2.4	1.32	1.33	1.36	1.39	1.52	1.72	1.90	2.16	2.81	3.75	5.52
0.1	3.6	1.45	1.46	1.49	1.52	1.65	1.82	1.99	2.23	2.81	3.65	5.21
0.1	5.5	1.60	1.61	1.64	1.67	1.79	1.95	2.11	2.34	2.87	3.62	5.00
0.1	8.5	1.77	1.78	1.80	1.83	1.94	2.10	2.25	2.47	2.97	3.67	4.91
0.1	13	1.94	1.95	1.97	2.00	2.11	2.25	2.40	2.61	3.11	3.77	4.92
0.1	20	2.12	2.13	2.16	2.19	2.30	2.42	2.57	2.78	3.28	3.92	5.00
10	1	1.18	1.20	1.23	1.27	1.47	1.81	2.12	2.58	3.63	5.07	7.45
10	1.5	1.27	1.29	1.32	1.36	1.52	1.82	2.08	2.47	3.40	4.68	6.96
10	2.4	1.40	1.41	1.44	1.48	1.63	1.86	2.08	2.41	3.18	4.26	6.24
10	3.6	1.51	1.53	1.55	1.59	1.72	1.93	2.12	2.40	3.07	4.02	5.73
10	5.5	1.65	1.66	1.69	1.72	1.85	2.02	2.19	2.45	3.04	3.86	5.34
10	8.5	1.81	1.82	1.84	1.88	1.99	2.15	2.31	2.54	3.08	3.81	5.09
10	13	1.97	1.98	2.01	2.04	2.15	2.29	2.44	2.67	3.18	3.86	5.02
10	20	2.15	2.16	2.18	2.22	2.32	2.45	2.60	2.82	3.33	3.99	5.07
1000	1	1.61	1.65	1.71	1.77	1.81	2.15	2.50	3.01	4.24	6.04	8.75
1000	1.5	1.65	1.68	1.73	1.78	1.87	2.18	2.50	2.98	4.14	5.91	9.34
1000	2.4	1.71	1.73	1.78	1.82	1.93	2.21	2.50	2.91	3.93	5.50	8.76
1000	3.6	1.78	1.80	1.84	1.87	1.99	2.24	2.50	2.87	3.77	5.11	7.86
1000	5.5	1.87	1.89	1.92	1.94	2.10	2.30	2.52	2.85	3.65	4.79	7.00
1000	8.5	1.99	2.00	2.02	2.05	2.19	2.38	2.58	2.88	3.59	4.58	6.39
1000	13	2.12	2.13	2.15	2.19	2.31	2.48	2.66	2.94	3.59	4.48	6.05
1000	20	2.27	2.27	2.29	2.34	2.45	2.61	2.78	3.04	3.65	4.47	5.85

Notes. Radii of planets, in $R_\oplus$. Column 1 is incident flux on the planet, relative to the solar constant. Column 2 is the total planet mass in $M_\oplus$. Otherwise, column headers indicate the fraction of a planet's mass in the H/He envelope.

rock/iron core. We do this because as $f_{\rm env}$ approaches zero, the planet radius does not approach zero but instead asymptotes to $R_{\rm core}$.

To a first order, however, the rock/iron EOS is very incompressible, and so we can approximate $R_{\rm core}$ with the mass–radius curve of an envelope-free rocky planet. Assuming an Earth-like rock/iron abundance, then $R_{\rm core}$ is described by Equation (2) to within ∼2%. If we also allow the iron fraction of the core to vary, then this error rises to ∼10%, but for the qualitative analysis we are attempting here such errors are unimportant. The term $M_{\rm core}$ in Equation (2) refers to the mass of the rock/iron core, which for sub-Neptune-sized planets is approximately the same as the total planet mass $M_{\rm p}$:

$$R_{\rm core} = \left(\frac{M_{\rm core}}{M_\oplus}\right)^{0.25} \approx \left(\frac{M_{\rm p}}{M_\oplus}\right)^{0.25}. \quad (2)$$

Likewise, we must make a small correction to account for the size of the radiative upper atmosphere. To a first approximation, this atmosphere is isothermal at the planet's equilibrium temperature $T_{\rm eq}$. For sub-Neptune-sized planets at several gigayears, the radiative–convective boundary is typically ∼100–1000 bar. For transiting planets, the broadband optical radius is typically ∼20 mbar, or ≈8–10 scale heights higher.

Table 3
Low-mass Planet Radii at 10 Gyr, Solar Metallicity

Flux ($F_\oplus$)	Mass ($M_\oplus$)	0.01%	0.02%	0.05%	0.1%	0.2%	0.5%	1%	2%	5%	10%	20%
0.1	1	1.08	1.10	1.13	1.17	1.22	1.37	1.53	1.75	2.25	2.94	4.14
0.1	1.5	1.19	1.20	1.23	1.27	1.31	1.45	1.60	1.81	2.28	2.93	4.05
0.1	2.4	1.32	1.34	1.37	1.40	1.45	1.58	1.71	1.90	2.35	2.95	3.98
0.1	3.6	1.45	1.47	1.49	1.53	1.58	1.70	1.82	2.01	2.44	3.01	3.97
0.1	5.5	1.60	1.62	1.64	1.67	1.75	1.84	1.96	2.15	2.56	3.11	4.03
0.1	8.5	1.77	1.78	1.80	1.84	1.91	2.00	2.13	2.31	2.72	3.25	4.14
0.1	13	1.94	1.95	1.97	2.00	2.09	2.17	2.30	2.48	2.90	3.44	4.31
0.1	20	2.12	2.14	2.16	2.19	2.25	2.36	2.49	2.68	3.10	3.65	4.53
10	1	1.23	1.25	1.28	1.31	1.44	1.68	1.87	2.17	2.84	3.70	5.11
10	1.5	1.31	1.33	1.36	1.40	1.49	1.72	1.90	2.19	2.83	3.66	5.03
10	2.4	1.43	1.44	1.47	1.51	1.60	1.78	1.96	2.21	2.80	3.58	4.89
10	3.6	1.54	1.55	1.58	1.62	1.73	1.87	2.03	2.27	2.81	3.53	4.75
10	5.5	1.67	1.69	1.71	1.75	1.85	1.98	2.13	2.35	2.86	3.52	4.64
10	8.5	1.82	1.84	1.86	1.90	1.98	2.11	2.25	2.47	2.95	3.58	4.61
10	13	1.98	1.99	2.02	2.05	2.13	2.26	2.40	2.61	3.07	3.68	4.66
10	20	2.16	2.17	2.20	2.23	2.32	2.43	2.56	2.77	3.23	3.83	4.77
1000	1	1.76	1.81	1.88	1.96	2.01	2.08	2.18	2.31	2.70	3.49	4.88
1000	1.5	1.77	1.81	1.88	1.94	1.99	2.08	2.17	2.33	2.91	3.76	5.36
1000	2.4	1.82	1.85	1.90	1.95	2.00	2.08	2.22	2.49	3.10	3.94	5.55
1000	3.6	1.87	1.90	1.94	1.98	2.03	2.12	2.30	2.58	3.20	4.03	5.54
1000	5.5	1.95	1.97	2.01	2.04	2.10	2.21	2.38	2.64	3.26	4.08	5.49
1000	8.5	2.05	2.07	2.10	2.12	2.19	2.31	2.48	2.73	3.31	4.10	5.44
1000	13	2.17	2.18	2.21	2.23	2.34	2.43	2.59	2.83	3.38	4.13	5.40
1000	20	2.31	2.32	2.34	2.36	2.47	2.57	2.72	2.95	3.49	4.20	5.38

Notes. Radii of planets, in $R_\oplus$. Column 1 is incident flux on the planet, relative to the solar constant. Column 2 is the total planet mass in $M_\oplus$. Otherwise, column headers indicate the fraction of a planet's mass in the H/He envelope.

Thus the size of the radiative atmosphere is approximately given by Equation (3), where g is a planet's gravity and $\mu_{\rm H/He}$ is the mean molecular weight. Generally, however, this correction is typically quite small ($\sim$0.1 $R_\oplus$) except at the very highest levels of irradiation:

$$R_{\rm atm} \approx \log\left(\frac{100\,{\rm bar}}{20\,{\rm mbar}}\right) H \approx 9\left(\frac{k_{\rm b}\,T_{\rm eq}}{g\,\mu_{\rm H/He}}\right). \quad (3)$$

With Equations (2) and (3) in place, we can now fit for $R_{\rm env}$ and then simply add $R_{\rm core}$ and $R_{\rm atm}$ to get the total radius. The results of these fits are summarized in Figure 2 and Equation (4).

Figure 2 compares our power-law fits to the results of our full models for representative values of $M_{\rm p}$, $f_{\rm env}$, $F_\oplus$, and age. The error bars in each panel show the 1σ scatter about the power-law fits for the full suite of models in our parameter study. Remarkably, this simple power-law description does a reasonable job of reproducing the results of our full model. In general, the analytic formulation in Equation (4) matches our full models to within $\sim$0.1 dex.

For the age evolution, we fit separate power laws for solar metallicity and enhanced-opacity models. The solar metallicity models cool more rapidly initially. As a result, they are already relatively cold by $\sim$100 Myr, and so the subsequent contraction

Table 4
Low-mass Planet Radii at 100 Myr, Enhanced Opacity

Flux ($F_\oplus$)	Mass ($M_\oplus$)	0.01%	0.02%	0.05%	0.1%	0.2%	0.5%	1%	2%	5%	10%	20%
0.1	1	1.25	1.17	1.19	1.24	1.43	1.89	2.57	3.00	4.32	6.81	11.7
0.1	1.5	1.31	1.25	1.28	1.31	1.47	1.93	2.58	3.17	3.97	6.18	10.6
0.1	2.4	1.42	1.37	1.41	1.44	1.60	2.14	2.51	3.11	4.30	5.36	9.05
0.1	3.6	1.53	1.49	1.52	1.57	1.71	2.18	2.51	3.02	4.31	5.57	7.86
0.1	5.5	1.66	1.63	1.67	1.72	1.84	2.23	2.53	2.97	4.09	5.69	7.25
0.1	8.5	1.82	1.79	1.82	1.87	2.00	2.33	2.57	2.95	3.90	5.29	7.73
0.1	13	1.97	1.96	1.99	2.04	2.16	2.45	2.67	3.00	3.81	4.99	7.25
0.1	20	2.15	2.14	2.17	2.23	2.33	2.58	2.79	3.10	3.82	4.82	6.68
10	1	1.34	1.25	1.29	1.35	1.53	2.05	2.79	3.12	4.72	7.13	11.1
10	1.5	1.38	1.33	1.37	1.41	1.58	2.07	2.80	3.41	4.31	6.47	10.4
10	2.4	1.47	1.44	1.48	1.51	1.68	2.25	2.67	3.32	4.50	5.67	9.14
10	3.6	1.58	1.54	1.58	1.64	1.77	2.26	2.62	3.17	4.55	5.71	8.11
10	5.5	1.70	1.67	1.71	1.77	1.89	2.30	2.60	3.07	4.27	5.94	7.30
10	8.5	1.85	1.83	1.86	1.92	2.04	2.37	2.63	3.01	4.01	5.50	7.98
10	13	1.99	1.99	2.02	2.08	2.19	2.48	2.70	3.04	3.88	5.12	7.50
10	20	2.17	2.17	2.19	2.25	2.35	2.61	2.82	3.13	3.87	4.90	6.81
1000	1	1.59	1.63	1.70	1.75	1.88	2.42	3.13	3.99	6.21	8.88	11.3
1000	1.5	1.63	1.67	1.72	1.77	1.90	2.46	3.25	3.84	6.01	9.41	14.0
1000	2.4	1.70	1.72	1.77	1.81	1.97	2.63	3.13	3.89	5.35	8.59	15.4
1000	3.6	1.77	1.79	1.83	1.87	2.02	2.57	3.01	3.67	5.23	7.27	13.4
1000	5.5	1.87	1.88	1.92	1.96	2.10	2.54	2.90	3.46	4.89	6.68	10.3
1000	8.5	1.99	2.00	2.03	2.08	2.21	2.56	2.86	3.31	4.48	6.23	8.82
1000	13	2.12	2.12	2.15	2.21	2.32	2.63	2.89	3.27	4.22	5.64	8.36
1000	20	2.27	2.27	2.30	2.36	2.47	2.73	2.95	3.30	4.12	5.28	7.38

Notes. Radii of planets, in $R_\oplus$. Column 1 is incident flux on the planet, relative to the solar constant. Column 2 is the total planet mass in $M_\oplus$. Otherwise, column headers indicate the fraction of a planet's mass in the H/He envelope.

is slower. However, the enhanced-opacity models must eventually cool, and by several gigayears any differences are erased. We fit power laws only to the evolution after 100 Myr. For solar metallicity $R_{\rm env} \sim t^{0.11}$, while for enhanced opacity $R_{\rm env} \sim t^{0.18}$. Equation (4) shows the results for the enhanced-opacity models:

$$R_{\rm env} = R_{\rm p} - R_{\rm core} - R_{\rm atm} = 2.06\, R_\oplus \left(\frac{M_{\rm p}}{M_\oplus}\right)^{-0.21} \times \left(\frac{f_{\rm env}}{5\%}\right)^{0.59} \left(\frac{F_{\rm p}}{F_\oplus}\right)^{0.044} \left(\frac{age}{5\,{\rm Gyr}}\right)^{-0.18}. \quad (4)$$

It is important to note, however, that the results of these fits are only meant to be a rough approximation of the full models summarized in Figure 1 and Tables 1–5. These fits are done purely to help understand the qualitative behavior of our thermal evolution models, not to be used in place of the full models. Also, Equation (4) only shows the fit to our enhanced-opacity models. At late times the solar metallicity models have a slightly shallower dependence on age, due to more rapid cooling at early ages.

Nonetheless, Equations (2) and (4) do make several things quite clear. First of all, we can now quantify the importance of H/He envelope fraction; doubling $f_{\rm env}$ has an order of

Table 5
Low-mass Planet Radii at 1 Gyr, Enhanced Opacity

Flux ($F_\oplus$)	Mass ($M_\oplus$)	0.01%	0.02%	0.05%	0.1%	0.2%	0.5%	1%	2%	5%	10%	20%
0.1	1	1.07	1.09	1.12	1.15	1.37	1.68	1.98	2.43	3.11	4.26	6.74
0.1	1.5	1.18	1.19	1.22	1.26	1.45	1.74	1.99	2.38	3.27	3.96	6.10
0.1	2.4	1.32	1.33	1.36	1.39	1.60	1.82	2.05	2.38	3.22	4.23	5.52
0.1	3.6	1.45	1.46	1.49	1.52	1.71	1.90	2.10	2.42	3.15	4.25	5.62
0.1	5.5	1.60	1.61	1.64	1.67	1.85	2.02	2.19	2.47	3.16	4.13	5.84
0.1	8.5	1.77	1.78	1.80	1.84	1.99	2.15	2.32	2.57	3.19	4.09	5.74
0.1	13	1.94	1.95	1.97	2.01	2.15	2.30	2.46	2.70	3.28	4.11	5.58
0.1	20	2.12	2.13	2.16	2.21	2.32	2.46	2.62	2.86	3.42	4.17	5.56
10	1	1.18	1.20	1.23	1.27	1.50	1.84	2.20	2.72	3.63	5.07	7.45
10	1.5	1.27	1.29	1.32	1.36	1.56	1.87	2.16	2.60	3.58	4.68	6.96
10	2.4	1.40	1.41	1.44	1.48	1.68	1.92	2.17	2.54	3.47	4.52	6.24
10	3.6	1.51	1.53	1.55	1.59	1.77	1.98	2.20	2.54	3.34	4.53	5.85
10	5.5	1.65	1.66	1.69	1.72	1.90	2.07	2.27	2.56	3.31	4.36	6.14
10	8.5	1.81	1.82	1.84	1.89	2.03	2.20	2.37	2.64	3.31	4.27	5.99
10	13	1.97	1.98	2.01	2.05	2.18	2.34	2.50	2.76	3.37	4.24	5.76
10	20	2.15	2.16	2.18	2.24	2.36	2.49	2.65	2.90	3.49	4.27	5.68
1000	1	1.61	1.65	1.71	1.77	1.85	2.20	2.60	3.09	4.24	6.04	8.75
1000	1.5	1.65	1.68	1.73	1.78	1.88	2.24	2.59	3.10	4.14	5.91	9.34
1000	2.4	1.71	1.73	1.78	1.82	1.96	2.26	2.57	3.02	4.13	5.50	8.76
1000	3.6	1.78	1.80	1.84	1.87	2.02	2.27	2.54	2.96	3.94	5.34	7.86
1000	5.5	1.87	1.89	1.92	1.94	2.11	2.32	2.54	2.90	3.80	5.05	7.13
1000	8.5	1.99	2.00	2.02	2.05	2.21	2.39	2.59	2.90	3.68	4.81	6.84
1000	13	2.12	2.13	2.15	2.19	2.32	2.49	2.67	2.96	3.65	4.65	6.41
1000	20	2.27	2.27	2.29	2.34	2.46	2.61	2.78	3.06	3.70	4.57	6.14

Notes. Radii of planets, in $R_\oplus$. Column 1 is incident flux on the planet, relative to the solar constant. Column 2 is the total planet mass in $M_\oplus$. Otherwise, column headers indicate the fraction of a planet's mass in the H/He envelope.

magnitude larger effect on R_p than doubling F_p and more than twice as large as the effect of doubling the age. We can also now see how flat the mass–radius curves are. Although R_{env} decreases slightly with mass, this is almost exactly balanced by the increase in R_{core} with increasing mass. This result is insensitive to our choice of initial entropy for ages $\gtrsim$10 Myr.

3.2. Why Is the Mass–Radius Relation Flat?

One of the key features of our thermal evolution and structure models is the relative flatness of mass–radius curves at fixed H/He envelope fraction. In Sections 3 and 3.1, we showed that for planets with $\gtrsim$1% H/He, planet size is more or less independent of mass. Thus far, however, we have not explained the origin of this flatness.

In fact, a search through the literature will show a wide range of mass–radius curves with very different behavior at low masses (e.g., Lissauer et al. 2011; Rogers et al. 2011; Lopez et al. 2012). Although all of the models tend to agree above $\sim$10–20 $M_\oplus$, there can be large disagreements below $\sim$5 $M_\oplus$. In some cases, radius decreases with decreasing mass in much the same way as the Earth-like mass–radius curves in Figure 1. In other cases, the radius increases to implausibly large sizes due to the planet's lower gravity (Rogers et al. 2011). Generally, these models face

Table 6
Low-mass Planet Radii at 10 Gyr, Enhanced Opacity

Flux ($F_\oplus$)	Mass ($M_\oplus$)	0.01%	0.02%	0.05%	0.1%	0.2%	0.5%	1%	2%	5%	10%	20%
0.1	1	1.08	1.10	1.13	1.17	1.24	1.37	1.53	1.75	2.32	2.97	4.14
0.1	1.5	1.19	1.20	1.23	1.27	1.34	1.46	1.61	1.82	2.33	3.04	4.05
0.1	2.4	1.32	1.34	1.37	1.40	1.47	1.57	1.71	1.92	2.40	3.07	4.13
0.1	3.6	1.45	1.47	1.49	1.53	1.59	1.70	1.83	2.01	2.49	3.12	4.23
0.1	5.5	1.60	1.62	1.64	1.67	1.76	1.85	1.97	2.16	2.59	3.22	4.27
0.1	8.5	1.77	1.78	1.80	1.84	1.88	2.02	2.14	2.32	2.75	3.34	4.37
0.1	13	1.94	1.95	1.97	2.00	2.10	2.18	2.30	2.50	2.93	3.50	4.51
0.1	20	2.12	2.14	2.16	2.19	2.27	2.37	2.49	2.69	3.13	3.71	4.66
10	1	1.23	1.25	1.28	1.31	1.39	1.55	1.75	2.02	2.72	3.70	5.11
10	1.5	1.31	1.33	1.36	1.40	1.48	1.62	1.79	2.05	2.66	3.57	5.03
10	2.4	1.43	1.44	1.47	1.51	1.58	1.70	1.85	2.10	2.65	3.44	4.89
10	3.6	1.54	1.55	1.58	1.62	1.69	1.80	1.94	2.15	2.69	3.41	4.67
10	5.5	1.67	1.69	1.71	1.75	1.84	1.93	2.07	2.27	2.75	3.44	4.61
10	8.5	1.82	1.84	1.86	1.90	1.98	2.08	2.21	2.41	2.86	3.51	4.62
10	13	1.98	1.99	2.02	2.05	2.14	2.23	2.36	2.56	3.02	3.63	4.70
10	20	2.16	2.17	2.20	2.23	2.31	2.41	2.54	2.74	3.21	3.81	4.81
1000	1	1.76	1.81	1.88	1.96	2.01	2.08	2.16	2.29	2.60	3.49	4.88
1000	1.5	1.77	1.81	1.88	1.94	1.99	2.05	2.15	2.28	2.83	3.72	5.36
1000	2.4	1.82	1.85	1.90	1.95	1.99	2.05	2.14	2.36	3.01	3.89	5.55
1000	3.6	1.87	1.90	1.94	1.98	2.02	2.09	2.18	2.42	3.10	3.97	5.48
1000	5.5	1.95	1.97	2.01	2.04	2.09	2.15	2.31	2.54	3.14	4.01	5.47
1000	8.5	2.05	2.07	2.10	2.12	2.15	2.28	2.43	2.67	3.21	4.01	5.40
1000	13	2.17	2.18	2.21	2.23	2.28	2.40	2.55	2.79	3.33	4.05	5.35
1000	20	2.31	2.32	2.34	2.36	2.45	2.55	2.69	2.92	3.45	4.15	5.32

Notes. Radii of planets, in $R_\oplus$. Column 1 is incident flux on the planet, relative to the solar constant. Column 2 is the total planet mass in $M_\oplus$. Otherwise, column headers indicate the fraction of a planet's mass in the H/He envelope.

one of two limitations. Either they ignore the contributions of the rock/iron core to the thermal evolution, i.e., the need to cool the core and heating from radioactive decay, or they do not perform an evolution calculation at all and instead use static structure models in which the internal energy of the planet is treated as a free parameter.

For the Neptune- and sub-Neptune-sized planets that we are focusing on here, ~90%–99% of a planet's mass is contained in the rock/iron core. Ignoring the effects of that core on the thermal evolution will significantly underestimate these planets cooling timescale and therefore the radius. This is a common simplification with thermal evolution models that, like our own, were originally developed to model massive gas giants, where the core has a negligible impact on the overall thermal evolution. The importance of these effects, however, is clearly demonstrated in Figure 3, which shows the various contributions to the overall thermal evolution for a typical 5 $M_\oplus$, 1% H/He, sub-Neptune-sized planet. At every age, the cooling luminosity of the planet is dominated by these core cooling and heating terms. At early times, the thermal evolution is largely regulated by the need to cool the rock/iron core with its relatively large heat capacity (Alfè et al. 2002; Guillot et al. 1995). At ages

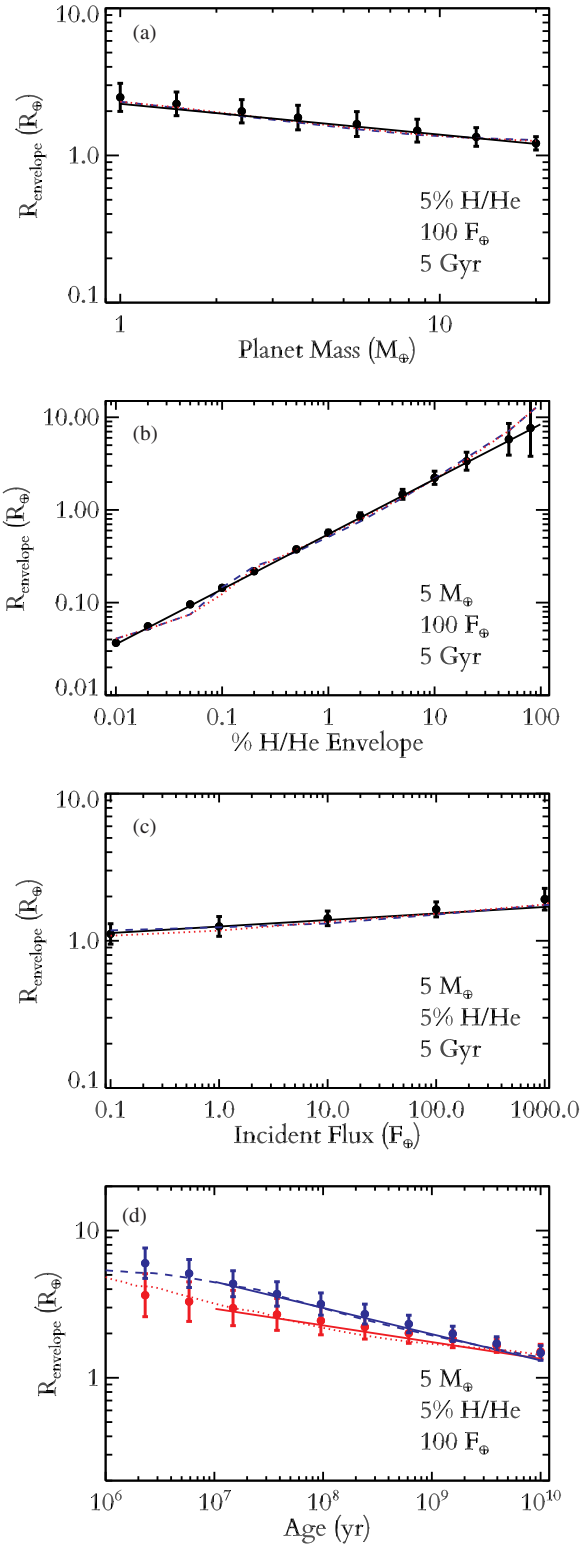

Figure 2. Four panels showing how the radius of the H/He envelope $R_{\rm env} = R_{\rm p} - R_{\rm core} - R_{\rm atm}$ varies with planet mass, envelope mass fraction, incident flux, and planet age for representative values. Red dotted lines correspond to solar metallicity atmospheres, and blue dashed lines correspond to enhanced opacity. Solid lines indicate power-law fits as described in Equation (4). Here we use default values of 5 $M_\oplus$, 100 $F_\oplus$, 5% H/He, and 5 Gyr.

(A color version of this figure is available in the online journal.)

$\gtrsim$1 Gyr, radioactive heating also becomes comparable to the core cooling rate, thanks mostly due to the decay of ^{40}K (Anders & Grevesse 1989). On the other hand, ignoring these terms leads

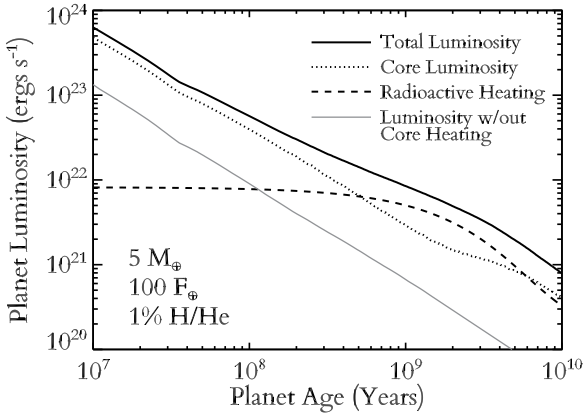

Figure 3. Here we show the planet luminosity budget vs. time for a representative example thermal evolution model with 1% H/He on a 5 $M_\oplus$ planet, receiving 100 $F_\oplus$ from a sun-like star. The black solid line shows the overall cooling rate, and the dotted and dashed lines show the cooling rate of the rock/iron core and the heating from radioactive decay, respectively. The solid gray line shows the cooling rate if we ignore radioactivity and the need to cool the core. This clearly demonstrates the need to include these terms when calculating the thermal evolution of sub-Neptune-like planets.

to a planet that is ~30–100 times less luminous at late times and underestimates the final radius by ~0.5 $R_\oplus$. Some models (e.g., Mordasini et al. 2012) make the compromise of including radiogenic heating but not including the effect of the core's heat capacity. This is much better than ignoring the core altogether, but as shown in Figure 3 both terms are important, and this will lead to underestimating the radii of sub-Neptune planets, especially at ages $\lesssim$1 Gyr.

On the other hand, it is also quite common to use static internal structure models that do not track a planet's thermal evolution but instead assume a fixed specific luminosity (i.e., power per unit mass), which is then treated as a free variable (Rogers et al. 2011). This is a common simplification made when a small H/He envelope is added to detailed models of terrestrial planets, for which the cooling history is harder to determine and has little impact on overall planet size (Valencia et al. 2007). When calculating possible envelope fractions for a single planet (e.g., Rogers & Seager 2010b), this is fine as long as the resulting uncertainty in the internal energy is accounted for. However, when plotting isocomposition mass–radius curves, this leads to an unphysical upturn at low masses. Lower-mass planets will of course have lower gravities and larger scale heights, so assigning them the same specific luminosities as more massive planets will lead to much larger envelopes.

In reality though, lower-mass planets tend to be colder at almost all ages. Partly this is due to their low gravities, which slightly increase the rate of radiative transfer through their atmospheres (Fortney et al. 2007). Mostly, however, it is simply due to the fact that lower-mass planets have a higher ratio of radiating surface areas to their total internal energies. Thermal evolution will naturally result in planets that have cooling timescales comparable to their ages. All other things being equal, lower-mass planets will have shorter cooling timescales; their H/He envelopes will cool and contract slightly more to compensate.

These results are summarized in Figures 4 and 5. Figure 4 shows various cooling curves for the internal entropy in the H/He envelope. Planets start with large initial entropy and therefore radii. As expected, models cool rapidly until their cooling timescale is comparable to their age. As in Figure 2, solar metallicity models cool rapidly for their first ~10 Myr

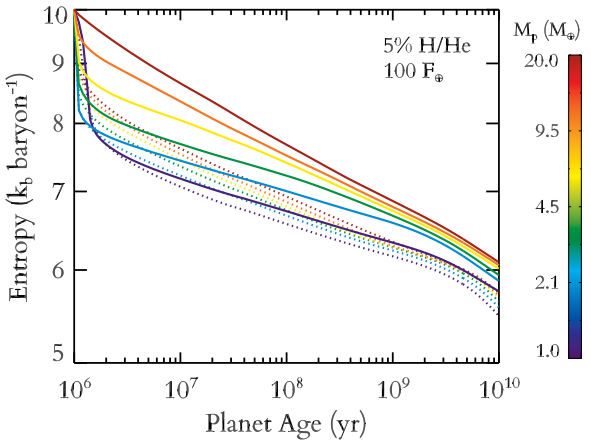

Figure 4. Shown is an example calculation in which all models start at the same young age and initial specific entropy. Internal specific entropy in the H/He envelope vs. time is shown for various planet masses. Solid lines show enhanced opacity, while dotted lines show solar metallicity. Planets start with large initial entropy, then rapidly cool. By 10–100 Myr, the models are insensitive to the choice of initial entropy. Low-mass planets experience more rapid cooling, leading to the flat mass–radius curves seen in Figure 1. Solar metallicity models cool rapidly at young ages and then experience more gradual cooling, while enhanced-opacity models cool more steadily at all ages.

(A color version of this figure is available in the online journal.)

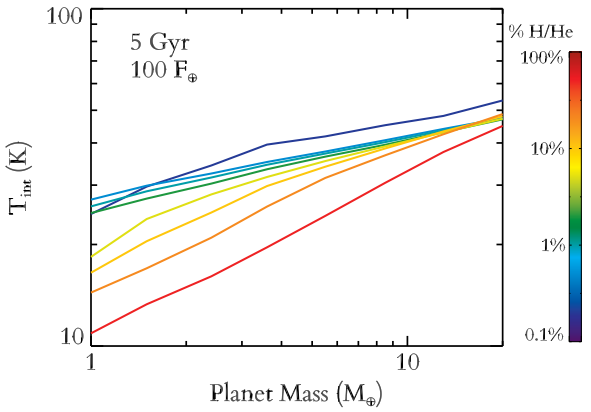

Figure 5. Intrinsic temperature $T_{\rm int}$, i.e., the equivalent blackbody temperature of a planet's net outgoing flux, vs. planet mass for 5 Gyr old planets receiving 100 $F_\oplus$ with enhanced-opacity atmospheres. Colors show different H/He envelope fractions. Clearly, by several gigayears, lower-mass planets are significantly colder than higher-mass planets. This demonstrates the need to perform full thermal evolution calculations. Simply assuming a fixed luminosity per mass will greatly overestimate the size of planets below $\sim$5 $M_\oplus$.

(A color version of this figure is available in the online journal.)

and then contract more slowly. The enhanced-opacity models, on the other hand, cool more steadily throughout their history. Eventually, the enhanced-opacity models must also cool and contract, and by several gigayears they have largely erased any differences with the solar models. At the same time, there is a slight change in the cooling rates due to the decay of ^{40}K.

Figure 5 shows the end result of this evolution. Here we show planetary intrinsic temperature $T_{\rm int}$ versus planet mass for various H/He envelope fractions for 5 Gyr old planets receiving 100 $F_\oplus$. As we can see, by 5 Gyr, low-mass planets are always significantly cooler than higher-mass planets at the same envelope fractions, regardless of H/He fraction or atmosphere metallicity.

Combined with the fact that lower-mass planets have slightly smaller rock/iron cores (Equation (2)), this increase in cooling counterbalances the fact that lower-mass planets have lower

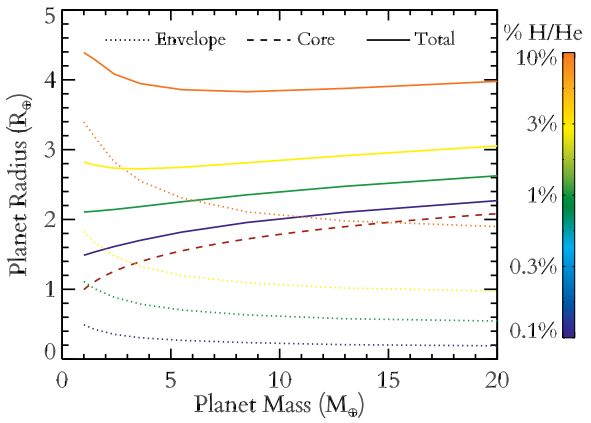

Figure 6. Here we show isocomposition mass–radius curves for 1–20 $M_\oplus$. The dashed rust-colored line shows the mass–radius relation for Earth-like bare rock and iron planets. Dotted lines show the thickness of the H/He envelope, and solid lines show the total planet radius, each color-coded by H/He envelope fraction. This show that for envelope fraction $\gtrsim$1% the downturn in radius for rocky planets at low mass is roughly balanced by the slight upturn in the thickness of H/He envelopes, leading to an overall flat mass–radius relationship.

(A color version of this figure is available in the online journal.)

gravities and produces the flat mass–radius curves seen in Figure 1. So long as a planet has enough of an envelope that $R_{\rm env} \gtrsim R_{\rm core}$, then Equations (2) and (4) will roughly balance and isocomposition mass–radius curves will be quite flat,as illustrated in Figure 6. This typically happens for planets that are $\gtrsim$1% H/He or $\gtrsim$2.5 $R_\oplus$. Thus for most of *Kepler*'s Neptune- and sub-Neptune-sized planets, radius is nearly independent of planet mass and is instead a direct measure of bulk H/He envelope fraction.

It has of course long been known that the mass–radius relationship should be flat for noninflated giant planets (e.g., Fortney et al. 2007). What is remarkable here is that this is true even when the H/He envelope is a small fraction of a planet's mass. Moreover, it is for a different reason than in giant planets. For Jupiter-mass planets and brown dwarfs, the mass–radius relationship is flat because their interiors are highly degenerate and partially ionized (e.g., Zapolsky & Salpeter 1969). That is not the case here, at the pressures and temperatures relevant for the interiors of Neptunes and sub-Neptunes, generally $\lesssim$1 Mbar and 10^4 K, as the envelope is generally not degenerate. Even at the base of the H/He envelope for a 20 $M_\oplus$ planet with a 20% envelope, the interior is only weakly degenerate: $\Theta = k_{\rm B}\hbar^2 2m_{\rm e}(3\pi)^{2/3}T/n_{\rm e}^{2/3} \sim 1$ (Nettelmann et al. 2008).

4. THE MASS–COMPOSITION RELATION

Using our thermal evolution and structure models, we calculated H/He envelope fractions for all $\sim$200 confirmed planets with well-determined masses, assuming a water-free interior. We excluded any planets that only have upper limits on mass or purely theoretical mass constraints. We used masses and radii from exoplanets.org (Wright et al. 2011), except for where there are more recent values in the literature. For CoRoT-7b, the five inner Kepler-11 planets, and 55 Cancri e, we used masses and radii from Hatzes et al. (2011), Lissauer et al. (2013), and Dragomir et al. (2013), respectively. We exclude confirmed planets with analytical TTV mass estimates from Xie et al. (2014) due to the degeneracy between planet mass and free eccentricity. For inflated hot Jupiters with radii larger than that of pure H/He, we simply assigned 100% H/He because such planets are beyond the scope of this work. Meanwhile, for potentially rocky

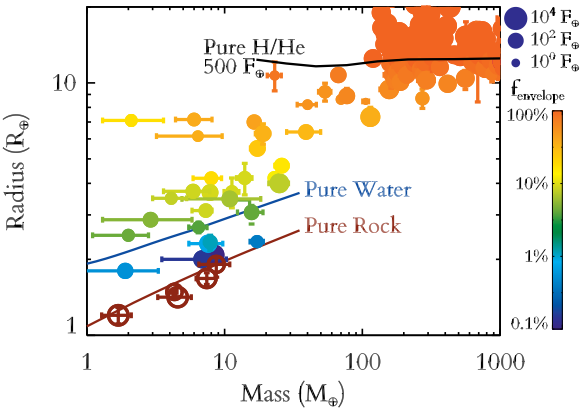

Figure 7. Planetary radius vs. mass for all 200 transiting planets with measured masses. Each planet is colored according to the fraction of its mass in an H/He envelope, assuming a water-free interior. Rust-colored open circles indicate potentially rocky planets. Points are sized according to the incident flux they receive from their parent stars, relative to $F_\oplus$, the flux that the Earth receives from the Sun. For comparison, we include theoretical mass–radius relations for pure silicate rock, pure water, and pure H/He at 500 $F_\oplus$. There is a very strong correlation between planetary radius and H/He envelope fraction, both of which are more weakly correlated with mass up to $\sim$100 $M_\oplus$.

(A color version of this figure is available in the online journal.)

planets like CoRoT-7b (Léger et al. 2009; Queloz et al. 2009) and Kepler-10b (Batalha et al. 2011), we set strict upper limits on the size of any potential H/He envelope. Table 7 summarizes the results for 44 planets with measured masses $<$100 $M_\oplus$ and radii $<$12 $R_\oplus$.

In order to calculate the uncertainty of these envelope fractions we included the effects of 1σ variations in the observed planet masses, radii, ages, and levels of irradiation. In addition, we included theoretical uncertainties on core iron fraction, core heat capacity, atmospheric albedo, and so on, as described in Lopez et al. (2012). In general, uncertainties in the stellar radius and therefore the planetary radius are the dominant source of uncertainty. Typically this is followed by the unknown iron fraction in the core, which is typically equivalent to a 0.1 $R_\oplus$ uncertainty in the radius for low-mass planets.

Figure 7 plots the current measured mass–radius relation with 1σ uncertainties for all confirmed transiting planets with measured masses up to 1000 $M_\oplus$ and radii 20 $R_\oplus$. The color of each point shows the H/He envelope fractions calculated by our models. Rust-colored open circles show potentially volatile-free rocky planets. Meanwhile, the size of the points correspond to the incident flux that each planet receives from its parent star, relative to $F_\oplus$, the incident flux that the Earth receives from the Sun.

Finally, we include three theoretical isocomposition curves. The rust-colored curve shows pure silicate rock (specifically olivine). The dark-blue curve corresponds to pure water worlds on a 10 day orbit around a 5 Gyr old, Sun-like star; however, varying these details does not significantly change the curve. Finally, the black curve corresponds to pure H/He, hot Jupiters receiving 500 $F_\oplus$ (i.e., 500 times the current incident flux that the Earth receives from the Sun) from a 5 Gyr old, Sun-like star. Roughly speaking, this last curve forms the dividing line between the inflated and noninflated hot Jupiters.

Several features of the mass–radius relation are immediately apparent. As noted in Weiss et al. (2013), there is a roughly power-law increase in radius from $\sim$1–100 $M_\oplus$, above which radius saturates at approximately a Jupiter radius. Below $\sim$10 $M_\oplus$ there is a particularly large scatter in radius, with planets

Table 7
Confirmed Planets with Well-determined Masses Less than 100 $M_\oplus$

Planet Name	Mass ($M_\oplus$)	Radius ($R_\oplus$)	H/He Envelope Fraction
Kepler-78b	$1.69\pm^{0.41}_{0.41}$	$1.20\pm^{0.09}_{0.09}$	>0.01%
Kepler-11b	$1.90\pm^{1.40}_{1.00}$	$1.80\pm^{0.03}_{0.05}$	0.51% $\pm^{0.43\%}_{1.35\%}$
Kepler-11f	$2.00\pm^{0.80}_{0.90}$	$2.49\pm^{0.04}_{0.07}$	2.28% $\pm^{1.20\%}_{0.62\%}$
Kepler-51b	$2.10\pm^{1.50}_{0.80}$	$7.10\pm^{0.30}_{0.30}$	16.9%$\pm^{10.8\%}_{9.9\%}$
Kepler-11c	$2.90\pm^{2.90}_{1.60}$	$2.87\pm^{0.05}_{0.06}$	6.10% $\pm^{1.21\%}_{0.99\%}$
Kepler-79e	$4.10\pm^{1.20}_{1.10}$	$3.49\pm^{0.14}_{0.14}$	7.99% $\pm^{1.05\%}_{1.10\%}$
Kepler-36b	$4.46\pm^{0.30}_{0.30}$	$1.48\pm^{0.03}_{0.03}$	>0.04%
Kepler-10b	$4.51\pm^{1.24}_{1.24}$	$1.41\pm^{0.03}_{0.03}$	>0.01%
Kepler-79c	$5.90\pm^{1.90}_{2.30}$	$3.72\pm^{0.08}_{0.08}$	8.85% $\pm^{0.70\%}_{0.91\%}$
Kepler-79d	$6.00\pm^{2.10}_{1.60}$	$7.16\pm^{0.13}_{0.16}$	36.7% $\pm^{3.56\%}_{3.43\%}$
Kepler-87c	$6.40\pm^{3.20}_{3.20}$	$6.15\pm^{0.09}_{0.09}$	34.5% $\pm^{2.24\%}_{2.49\%}$
GJ1214b	$6.46\pm^{0.99}_{0.99}$	$2.67\pm^{0.12}_{0.12}$	3.83% $\pm^{1.30\%}_{7.13\%}$
Kepler-18b	$6.87\pm^{3.48}_{3.48}$	$2.00\pm^{0.09}_{0.09}$	0.31% $\pm^{0.76\%}_{0.67\%}$
Kepler-11d	$7.30\pm^{0.80}_{1.50}$	$3.12\pm^{0.06}_{0.07}$	4.57% $\pm^{1.04\%}_{1.00\%}$
CoRoT-7b	$7.42\pm^{1.21}_{1.21}$	$1.67\pm^{0.09}_{0.09}$	>0.03%
Kepler-68b	$7.59\pm^{2.06}_{2.06}$	$2.30\pm^{0.05}_{0.08}$	0.35% $\pm^{0.38\%}_{0.82\%}$
Kepler-68b	$7.60\pm^{2.10}_{2.10}$	$2.30\pm^{0.06}_{0.09}$	0.76% $\pm^{0.31\%}_{0.39\%}$
HD 97658b	$7.86\pm^{0.73}_{0.73}$	$2.34\pm^{0.18}_{0.15}$	0.99% $\pm^{1.01\%}_{1.80\%}$
Kepler-11e	$8.00\pm^{1.50}_{2.10}$	$4.19\pm^{0.07}_{0.09}$	15.0% $\pm^{1.70\%}_{1.65\%}$
Kepler-36c	$8.10\pm^{0.53}_{0.53}$	$3.67\pm^{0.05}_{0.05}$	7.80% $\pm^{1.07\%}_{1.03\%}$
55Cnce	$8.32\pm^{0.39}_{0.39}$	$1.99\pm^{0.08}_{0.08}$	0.14% $\pm^{0.21\%}_{0.37\%}$
Kepler-20b	$8.45\pm^{2.12}_{2.12}$	$1.90\pm^{0.11}_{0.20}$	>0.28%
Kepler-79b	$10.9\pm^{7.40}_{6.00}$	$3.47\pm^{0.07}_{0.07}$	6.56% $\pm^{0.74\%}_{0.98\%}$
GJ3470b	$13.9\pm^{1.63}_{1.63}$	$4.19\pm^{0.59}_{0.59}$	12.8% $\pm^{5.15\%}_{5.00\%}$
Kepler-20c	$15.7\pm^{3.31}_{3.31}$	$3.06\pm^{0.19}_{0.30}$	3.45% $\pm^{1.47\%}_{5.38\%}$
Kepler-18d	$16.3\pm^{1.39}_{1.39}$	$6.97\pm^{0.32}_{0.32}$	37.5% $\pm^{3.54\%}_{3.67\%}$
Kepler-10c	$17.2\pm^{1.9}_{1.9}$	$2.35\pm^{0.09}_{0.04}$	0.47% $\pm^{0.70\%}_{0.45\%}$
Kepler-18c	$17.2\pm^{1.90}_{1.90}$	$5.48\pm^{0.25}_{0.25}$	23.6% $\pm^{2.72\%}_{3.09\%}$
HAT-P-26b	$18.6\pm^{2.28}_{2.28}$	$6.33\pm^{0.58}_{0.58}$	31.7% $\pm^{6.20\%}_{6.04\%}$
GJ436b	$23.0\pm^{1.01}_{1.01}$	$4.22\pm^{0.09}_{0.10}$	12.0% $\pm^{1.20\%}_{2.12\%}$
Kepler-4b	$24.5\pm^{4.07}_{4.07}$	$4.00\pm^{0.21}_{0.21}$	7.70% $\pm^{1.64\%}_{2.18\%}$
HAT-P-11b	$26.2\pm^{2.86}_{2.86}$	$4.73\pm^{0.15}_{0.15}$	15.1% $\pm^{1.68\%}_{2.57\%}$

Table 7
(Continued)

Planet Name	Mass ($M_\oplus$)	Radius ($R_\oplus$)	H/He Envelope Fraction
WASP-77Ab	$37.9\pm^{6.88}_{6.88}$	$13.5\pm^{0.22}_{0.22}$	$100.\% \pm^{0.00\%}_{0.00\%}$
Kepler-35b	$40.3\pm^{6.35}_{6.35}$	$8.16\pm^{0.15}_{0.15}$	$47.0\% \pm^{1.96\%}_{2.96\%}$
Kepler-9c	$53.5\pm^{5.52}_{5.52}$	$9.22\pm^{0.75}_{0.75}$	$64.9\% \pm^{9.08\%}_{9.11\%}$
HAT-P-18b	$62.6\pm^{4.25}_{4.25}$	$11.1\pm^{0.58}_{0.58}$	$87.1\% \pm^{13.3\%}_{7.12\%}$
HAT-P-12b	$66.9\pm^{4.19}_{4.19}$	$10.7\pm^{0.32}_{0.23}$	$80.3\% \pm^{4.01\%}_{3.53\%}$
CoRoT-8b	$68.6\pm^{10.8}_{10.8}$	$6.38\pm^{0.22}_{0.22}$	$28.6\% \pm^{2.63\%}_{6.24\%}$
Kepler-34b	$69.9\pm^{3.49}_{3.17}$	$8.56\pm^{0.15}_{0.13}$	$53.2\% \pm^{1.90\%}_{4.09\%}$
WASP-29b	$77.2\pm^{6.39}_{6.39}$	$8.87\pm^{0.62}_{0.39}$	$60.0\% \pm^{7.57\%}_{6.07\%}$
Kepler-9b	$79.0\pm^{6.67}_{6.67}$	$9.43\pm^{0.77}_{0.77}$	$62.5\% \pm^{8.58\%}_{9.51\%}$
HAT-P-38b	$85.0\pm^{6.42}_{6.42}$	$9.24\pm^{1.03}_{0.70}$	$62.8\% \pm^{11.9\%}_{9.35\%}$
WASP-39b	$90.3\pm^{9.97}_{9.97}$	$14.2\pm^{0.44}_{0.44}$	$100.\% \pm^{0.00\%}_{0.00\%}$
HAT-P-19b	$92.8\pm^{5.58}_{5.58}$	$12.6\pm^{0.80}_{0.80}$	$100.\% \pm^{0.00\%}_{0.00\%}$
WASP-21b	$95.4\pm^{4.25}_{4.25}$	$11.9\pm^{0.67}_{0.67}$	$100.\% \pm^{0.00\%}_{16.6\%}$

Notes. Taken from exoplanets.org (Wright et al. 2011). Here we list each planets name, mass, radius, and the fraction of its mass in an H/He envelope according to our thermal evolution models. Planets with upper limits correspond to potentially rocky planets. The upper limit comes from the observed uncertainties on mass and radius and assumes a maximally iron-rich core (Marcus et al. 2010).

ranging from the potentially rocky to sub-Neptune-sized planets with ∼3% H/He. For low-mass planets there is also an inverse correlation between radius and incident flux, which may be due to photoevaporative loss of H/He (Lopez et al. 2012; Owen & Wu 2013).

Above ∼100 $M_\oplus$ we find the true gas giants, including the highly inflated hot Jupiters. Here the correlation with incident flux is the reverse of that at low mass with the most-irradiated planets being extremely inflated. It is unclear why there do not appear to be any super-inflated hot Jupiters below ∼100 $M_\oplus$; it is possible that such planets would be unstable to photoevaporation or Roche-lobe overflow (Jackson et al. 2010) or have a high-mass fraction of heavy elements (Miller & Fortney 2011).

Turning to the compositions of these planets, it is immediately clear that the H/He envelope fraction is strongly correlated with both planet mass and radius. However, on closer inspection, where there is scatter in the mass–radius relationship it is the planet radius that correlates with envelope fraction. We argue here that planet radius is first and foremost a proxy for a planet's H/He inventory. The fact that both envelope fraction and radius correlate with mass is due to the fact that more massive planets are able to accrete more gas during formation.

The radius saturates at ∼100 $M_\oplus$ because planet size does not simply increase with increasing H/He mass but rather with increasing H/He mass *fraction*. As shown in Section 3, there is an approximately power-law relationship between the size of a planet's H/He envelope and the planets H/He mass fraction. A 100 $M_\oplus$ planet with a 10 $M_\oplus$ core is already 95% H/He; as a result, doubling the planet's mass will not significantly increase the H/He envelope fraction or the radius.

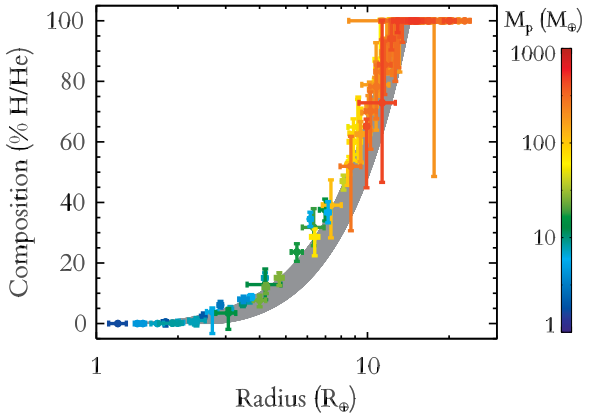

Figure 8. H/He envelope fraction vs. planet radius for the 200 transiting planets shown in Figure 7. Here each planet is color-coded according to its mass. The gray-shaded region shows the effect of varying the water abundance of the interior, which lowers the amount of H/He at a given radius. Clearly there is a very tight correlation between size and H/He envelope fraction, lending credence to our claim that radius can be used as a proxy for planetary composition.

(A color version of this figure is available in the online journal.)

Figure 8 shows the observed sample of transiting planets except that here we have plotted H/He envelope fraction against radius. This clearly demonstrates the close relationship between the observed radius and the fundamental bulk composition, i.e., the fraction of its mass in H/He versus heavy elements. At a given radius, planet mass, shown by the color bar, can span up to a factor of ∼30. Nonetheless, the scatter in H/He envelope fraction is typically only ∼0.3 dex. This is what we mean when we state that radius is primarily a proxy for composition.

Thus far, however, we have only considered dry interiors with H/He envelopes atop rock/iron cores. The gray-shaded region in Figure 8 shows the effect of varying the water abundance of planets in our model. Using our three-layer models, we varied the water abundance of the interior from completely dry, up to 90% of core mass, where by "core" we mean the combined mass of the rock and water layers. For clarity, we then fit power laws to best-fit radii and envelope fractions under both scenarios; the gray-shaded region shows the area in between these fits. Clearly, allowing this degeneracy does slightly increase the scatter in the radius–envelope fraction relationship. Nonetheless, above ∼3 $R_\oplus$ this does not alter the conclusion that radius and H/He envelope fraction are intimately related.

As a result, this means that we can recast the mass–radius relationship in Figure 7 as a mass–*composition* relationship. This is shown in Figure 9. By doing this we have transformed the observable mass–radius relationship into one that is directly relatable to models of planet formation. Here we can clearly see that there is a fundamental change in the relationship around ∼10 $M_\oplus$. Below this, planets typically have less than ∼5% of their mass in H/He with no clear relationship between envelope fraction and mass. Above this, however, most planets are roughly consistent with $\gtrsim$10 $M_\oplus$ of heavy elements, and we see a steady rise in envelope fraction from sub-Neptunes up to gas giants.

These trends are all understandable in light of the traditional core-accretion model of planet formation (e.g., Hayashi et al. 1985; Bodenheimer & Pollack 1986). If a planet's rocky core becomes sufficiently massive, typically ∼5–10 $M_\oplus$, then its gravity becomes sufficiently strong to trigger runaway accretion from the disk. For comparison, the dashed black line in Figure 9

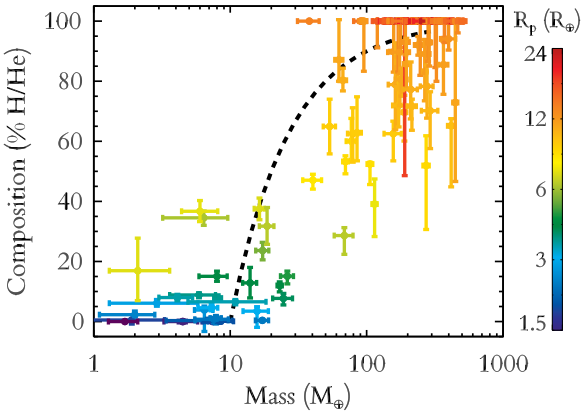

Figure 9. Similar to Figure 8 but with H/He envelope fraction plotted against planetary mass and color-coded by radius. Below ∼10 $M_\oplus$ there is a mix of rocky planets, possible water worlds, and sub-Neptunes with a few percent H/He. From ∼10–100 $M_\oplus$ there is a strong increase in both radii and H/He envelope fraction, transitioning from Neptune-sized planets with ∼10% H/He up to true gas giants that are almost entirely H/He. Above ∼100 $M_\oplus$ we find the familiar hot Jupiters, many of which have large, inflated radii. The dashed black line shows a toy model in which all planets have a 10 $M_\oplus$ core.

(A color version of this figure is available in the online journal.)

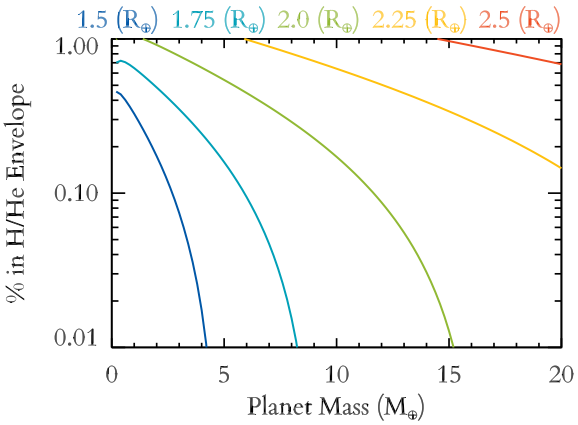

Figure 10. H/He envelope fraction vs. planet mass for super-Earth- and sub-Neptune-sized planets. Curves are color-coded according to planet radius, ranging from 1.5 to 2.5 $R_\oplus$. Here we assume water-free sub-Neptunes with H/He envelopes atop Earth-like rocky cores.

(A color version of this figure is available in the online journal.)

shows a simple toy model in which all planets have a 10 $M_\oplus$ core with solar metallicity H/He envelopes. This is of course a simplified view of planet formation. In reality there is considerable variation in disk mass, lifetime, metallicity, planet history, and so on, all of which introduces considerable scatter into the mass–envelope fraction relationship. Most planets in Figure 9 lie to the right of the toy model, possibly indicating that they accreted additional planetesimals embedded in the nebula (Mordasini 2013). Nonetheless, Figure 9 offers evidence for the core-accretion model of planet formation, at least for the close-in planets found by *Kepler*.

5. THE SUPER-EARTH TO SUB-NEPTUNE TRANSITION

Throughout this paper, we have repeatedly used the terms super-Earth and sub-Neptune to refer to low-mass *Kepler* planets. What exactly is the difference between these classes of planets? For our purpose a sub-Neptune is any planet whose radius cannot be explained by a bare rock/iron model; that is, it must have some sort of large, optically thick H/He or water envelope. Super-Earth on the other hand implies a more terrestrial planet, one that may have a solid or liquid surface and where the atmosphere, if any, contributes a negligible fraction to the planet's size. Although this may seem like semantics, one of the long-term goals of exoplanet science is to search for biomarkers in the transmission spectra of potentially habitable super-Earths. Whether or not a planet has a large H/He envelope tens of kilobars deep has very important implications for habitability.

The current definition used by the *Kepler* mission is that planets 1.5–2.0 $R_\oplus$ are super-Earths, while planets 2.0–4.0 $R_\oplus$, are sub-Neptunes. These round numbers, however, do not quite correspond to our more physically motivated definition of whether or not a planet has a thick envelope. Figure 10 plots the minimum H/He envelope fractions required by our models versus planet mass for several different radii in the 1.5–2.5 $R_\oplus$ super-Earth/sub-Neptune transition region.

It is quite difficult to construct a 2.0 $R_\oplus$ planet that does not have some sort of thick envelope. Assuming an Earth-like interior, such planets would have to be 16.5 $M_\oplus$ to explain their size without any type of envelope. For a completely iron-free interior, it is possible to construct a 2.0 $R_\oplus$ that is only 11 $M_\oplus$. However, completely iron-free is probably not a realistic composition for planets of several Earth masses. Indeed both Kepler-10b and CoRoT-7b may be slightly enhanced in iron compared to the Earth (Batalha et al. 2011; Hatzes et al. 2011).

This stands in contrast to the observed sample of likely rocky planets, all of which are <10 $M_\oplus$. It is possible that more massive rocky planets are yet to be found; however, the *Kepler* is essentially complete for 2.0 $R_\oplus$ within 100 days (Petigura et al. 2013b). For follow-up radial velocity and TTV mass measurements to have missed a population of <10 $M_\oplus$ rocky planets, they would need to somehow be biased against more massive and therefore easier-to-detect planets. Note that despite a density of 7.1 g cm^{-3} and a mass of 17.2 ± 1.9 $M_\oplus$, even Kepler-10c (Dumusque et al. 2014) is inconsistent with a volatile-free rocky planet; according to our models it would need 0.5% of its mass in an H/He envelope, similar to other sub-Neptunes like Kepler-11b. Moreover, there are basic arguments in core-accretion theory that lead us to expect that there should not be ∼20 $M_\oplus$ rocky planets. By the time a planet is ∼10 $M_\oplus$, its gravity should be sufficiently strong that it should be able to accrete a substantial H/He envelope from the disk (Ikoma & Hori 2012) and for periods $\gtrsim$10 days be able to retain it against photoevaporation (Lopez & Fortney 2013).

On the other hand, if we assume a more-typical low-mass planet with a 5 $M_\oplus$ Earth-like core, then to be 2.0 $R_\oplus$ it would need 0.5% of its mass in an H/He envelope. This may not sound like much, but it corresponds to ∼20 kbars of hydrogen and helium, ∼20 times higher than the pressure at the bottom of the Mariana Trench. Moreover, the temperature at the bottom of such an envelope would be $\gtrsim$3000 K, even for ages of several gigayears. We believe that such a planet is more properly classified as a sub-Neptune. As a result, 2.0 $R_\oplus$ is more of a quite hard upper limit for the size of an envelope-free super-Earth, and most of the planets between ∼1.75 and 2.0 $R_\oplus$ are likely to be H/He-rich sub-Neptunes.

If 2.0 $R_\oplus$ is really the hard upper limit for the super-Earth/sub-Neptune transition, then what is the lower limit? As shown in Figure 10, for planets $\lesssim$1.5 $R_\oplus$ it is entirely possible to explain their radii without any H/He. Moreover, if such planets do have any H/He, then it must be $\lesssim$0.1% of their mass, even if we

assume a maximally iron-rich core. This is small enough of an envelope that the rock/iron core dominates the planet's size. Moreover, as shown in Lopez & Fortney (2013) and Owen & Wu (2013), such tenuous envelopes are quite vulnerable to being completely photoevaporated, at least at periods $\lesssim$100 days. This does not exclude the possibility that 1.5 $R_\oplus$ cannot have large water envelopes, but it does suggest that they are unlikely to have large H/He envelopes.

To summarize, we can say that 2.0 $R_\oplus$ is likely a hard upper limit for the maximum size of envelope-free rocky super-Earths, and 1.5 $R_\oplus$ is likely a lower limit for the minimum size of an H/He-rich sub-Neptune. As a result, we suggest using $\sim$1.75 $R_\oplus$ rather than 2.0 $R_\oplus$ for the dividing line between these classes of planets.

6. DISCUSSION

In Sections 3 and 4, we showed that planetary radius is to a first order a proxy for a planet's envelope fraction above $\sim$2 $R_\oplus$. This means that the observed radius occurrence distribution for *Kepler* candidates found by Fressin et al. (2013) and Petigura et al. (2013b) is in reality an *envelope fraction* occurrence distribution for close-in planets at several gigayears. In particular, Fressin et al. (2013) and Petigura et al. (2013b) found that there is a sharp, roughly power-law-like drop-off in the frequency of planet occurrence above $\sim$3 $R_\oplus$, while below this there is a plateau in the planet occurrence rate down to at least 1 $R_\oplus$.

6.1. Planet Formation

This distribution makes sense in the light of traditional core-accretion theory. The timescale for planetesimal collisions to form rocky planets is short compared to the typical lifetime of a disk, and such planetesimals are preferentially concentrated deep in the star's potential well, so nature easily makes large populations of irradiated rocky planets (Chiang & Laughlin 2013; Hansen & Murray 2013).

At larger sizes, planets are limited by their ability to accrete an H/He envelope from the disk before the disk dissipates (Bodenheimer et al. 2000; Ikoma & Hori 2012; Mordasini et al. 2012). In these models the accretion of the envelope is limited by the ability of the protoplanetary envelope to cool and contract. This makes it difficult to accrete larger initial H/He envelopes, particularly if the *Kepler* population formed in situ (Ikoma & Hori 2012). It easier to form large planets farther out, particularly beyond the snow line where the increase in the local solid mass makes it easier to trigger runaway accretion to make a gas giant. The relative scarcity of hot Jupiters found by Fressin et al. (2013) and Petigura et al. (2013b) is an indication that whatever migration mechanism brings in gas giants to orbits $\lesssim$100 days must be fairly rare.

One key puzzle, however, is the location of the break in the planet occurrence rate distribution. If it were due to a transition from a large rocky population to a sub-Neptune population, with planet occurrence declining with increasing envelope fraction, then one would expect the break to occur at $\sim$1.5–1.8 $R_\oplus$, which we have concluded is likely the maximum size for bare rocky planets. Instead the break occurs at 2.8 $R_\oplus$, indicating that the occurrence plateau must include many volatile-rich planets. Although 2.8 $R_\oplus$ is far too large for bare rocky planets, it is achievable for H/He-free water worlds. A 10 $M_\oplus$ planet with 80% of its mass in a water envelope would be $\sim$2.7 $R_\oplus$. As a result, it is at least possible that the break in the planet occurrence distribution is a transition from an abundant population of rocky *and* water-rich planets to a population with accreted H/He envelopes. Otherwise, the models must explain why the plateau should include a substantial population of planets with $\sim$1%–3% of their mass in H/He envelopes before dropping off at larger envelope fractions.

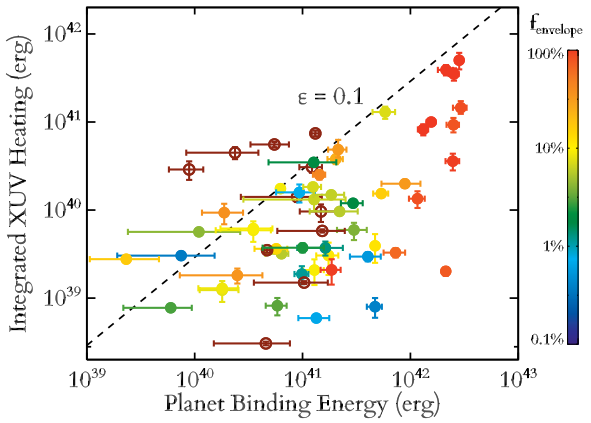

Figure 11. Updated version of the photoevaporation threshold diagram from Lopez et al. (2012) and Lissauer et al. (2013). Integrated extreme UV heating received by a planet over its lifetime (y axis) vs. current planetary binding energy (x axis) for all transiting planets with well-determined masses $\leqslant$100 $M_\oplus$, listed in Table 1. Points are color-coded by their H/He envelope fractions, with rust-colored open circles indicating rocky planets. For comparison, the dashed line is the expected evaporation threshold from the coupled thermal evolution and photoevaporation models of Lopez et al. (2012). There are no planets with significant H/He envelopes well above this threshold, indicating that the population of low-mass transiting planets has been significantly sculpted by photoevaporation.

(A color version of this figure is available in the online journal.)

One potential explanation is that perhaps the $\sim$2–3 $R_\oplus$ planets have hydrogen envelopes that were outgassed instead of accreted directly from the nebula. Elkins-Tanton & Seager (2008) showed that low-mass planets can outgas up to $\sim$5% of their mass after formation in H_2. However, this was only the case if the planetsinteriors were initially very wet, with about half the mass of their initial mantles in water. This again requires a large amount of water or other volatile ices to migrate to short-period orbits.

6.2. H/He Envelopes Sculpted by Photoevaporation

It is also important to note that although the observed radius distribution may tell us the envelope fraction distribution of *Kepler* candidates today, this is not the same as the initial distribution the planets formed with. As shown in Lopez et al. (2012), Lopez & Fortney (2013), and Owen & Wu (2013), the observed *Kepler* population has likely been significantly sculpted by photoevaporation. Close-in, low-mass planets have likely lost a significant fraction of their initial H/He inventories, resulting in smaller radii today. Furthermore, less-irradiated planets should be able to accrete larger initial H/He envelopes in the first place (Ikoma & Hori 2012). As more quarters of data are analyzed and the occurrence distribution pushes out to longer periods, there should be a distinct increase in the abundance of Neptune- and sub-Neptune-sized planets.

Figure 11 shows an updated version of the photoevaporation threshold diagram from Lopez et al. (2012) and Lissauer et al. (2013). This diagram compares the heating that a given planet receives from photoionizing radiation to the planet's current gravitational binding energy GM^2/R. This type of diagram was first proposed by Lecavelier Des Etangs (2007) for studying the effect of evaporation from hot Jupiters and has since become

a standard diagnostic tool for understanding the importance of evaporation (e.g., Lopez et al. 2012; Jackson et al. 2012; Owen & Jackson 2012; Lissauer et al. 2013; Zahnle & Catling 2013). For each planet, we compute the integrated extreme UV flux that a planet receives at its semimajor axis from when it was 10 Myr old until now. To estimate the XUV output from the star at ages >100 Myr we use the empirical scaling law $F_{\rm XUV} = 29.7\,({\rm age/Gyr})^{-1.23}(a/{\rm AU})^{-2}\,{\rm erg\,s^{-1}\,cm^{-2}}$ from Ribas et al. (2005); at earlier ages we assume that the XUV irradiation saturates as in Lopez et al. (2012) based on X-ray observations from Jackson et al. (2012). We then multiply this integrated XUV flux by the planet's current cross section, $\pi R_{\rm p}^2$.

In order to compare to a more detailed model, we include the expected evaporation threshold predicted by our coupled thermal evolution and evaporation model from Lopez et al. (2012). This accounts for changes in the planet's size over its lifetime due to both thermal evolution and evaporation. This model is defined by a photoevaporation efficiency ϵ, i.e., the fraction of the incident XUV flux that is converted into useful work to remove mass. That this threshold lies so close to the one-to-one line is a coincidence; the 10% evaporation efficiency is counterbalanced by the fact that the planets were two to three times larger when they were young and most of the evaporation was taking place (Lopez et al. 2012).

Figure 11 shows that the population of highly irradiated, low-mass planets have likely had their H/He envelope fractions, and therefore their radii, significantly sculpted by photoevaporation. It is worth noting that since we first published a version of this diagram in Lopez et al. (2012), the sample size has nearly doubled, including the discovery of extremely low-density planets like Kepler-79d (Jontof-Hutter et al. 2014). Nonetheless, there are still no observed transiting planets with substantial H/He envelopes that lie above the predicted evaporation threshold. Of the planets that do lie above the threshold, two, Kepler-10b and Kepler-78b, are likely rocky (Howard et al. 2013; Pepe et al. 2013), and the third, 55 Cancri e, likely has a steam envelope (Gillon et al. 2012). All three of these planets and many of the Earth-sized *Kepler* candidates are consistent with being the evaporated remnants of sub-Neptunes that initially had H/He envelopes.

Consequently, photoevaporation has important implications for current efforts to measure eta-Earth (e.g., Petigura et al. 2013a), the frequency of Earth-sized planets in the habitable zones of Sun-like stars. The *Kepler* survey is highly incomplete for Earth-sized planets on orbital periods longer than ∼200 days (e.g., Petigura et al. 2013b, 2013a). If most of *Kepler's* short-period, Earth-sized candidates are in fact the photoevaporated remnants of former sub-Neptunes, then current efforts to extrapolate the frequency of these candidates to longer orbital periods, where evaporation becomes much less effective (Owen & Jackson 2012), will significantly overestimate the frequency of Earth-sized planets.

Another potential effect of photoevaporation is the opening up of an "evaporation valley" in the radius–flux distribution (Lopez & Fortney 2013; Owen & Wu 2013). Photoevaporation makes it less likely that planets will survive with envelopes $\lesssim$1% of their mass if they are on highly irradiated orbits. Planets will tend to either retain more substantial envelopes or lose them entirely. More work needs to be done to carefully search for such a deficit; however, there are some preliminary indications that it may exist. Both the raw candidate distribution (Owen & Wu 2013) and a well-studied sample of M-dwarfs (Morton & Swift 2013) appear to show a slight dip in the frequency of planets at $\sim 2\,R_\oplus$. Such hints are still preliminary, but if real this has important implications for constraining the envelope fractions of the *Kepler* population because any large variation in the water fraction of close-in planets will tend to erase such a feature (Lopez & Fortney 2013). Using the models presented here, it is possible to instead study the *Kepler* envelope fraction distribution, which should aid in detecting any such "evaporation valley."

7. SUMMARY

One of the key strengths of the thermal evolution models used here is that they allow us to predict the radius of a planet as a function of mostly observable parameters, namely, planet mass, incident flux, age, and envelope fraction. For Neptune- and sub-Neptune-sized planets, we showed in Section 3 that the effect of varying planet mass or incident flux on the radius is an order of magnitude smaller than the effect of varying the fraction of a planet's mass in an H/He envelope. In Section 3.2, we described how this flatness in isocomposition mass–radius curves arises as a natural result of our thermal evolution models. As a result of these features, planetary radius is to a first order a proxy for the H/He inventory of sub-Neptune and larger planets, almost independent of their mass. In Section 4 we showed the close connection between radius and envelope fraction for the observed population of transiting planets with measured masses. We then demonstrated how our models allow us to recast the observed mass–radius distribution as a mass–composition relationship, allowing a more direct comparison to models of planet formation and evolution.

E.D.L. would like to thank Jack Lissauer, Angie Wolfgang, Caroline Morley, Nadine Nettelmann, Lauren Weiss, and Leslie Rogers for many helpful conversations. This research has made use of the Exoplanet Orbit Database and the Exoplanet Data Explorer at exoplanets.org. We acknowledge the support of NASA grant NNX09AC22G, NSF grant AST-1010017, and the UCSC Chancellor's Dissertation Year Fellowship.

REFERENCES

Alfè, D., Price, G. D., & Gillan, M. J. 2002, PhRvB, 65, 165118
Anders, E., & Grevesse, N. 1989, GeCoA, 53, 197
Baraffe, I., Alibert, Y., Chabrier, G., & Benz, W. 2006, A&A, 450, 1221
Batalha, N. M., Borucki, W. J., Bryson, S. T., et al. 2011, ApJ, 729, 27
Batalha, N. M., Rowe, J. F., & Bryson, S. T. 2013, ApJS, 204, 24
Bodenheimer, P., Hubickyj, O., & Lissauer, J. J. 2000, Icar, 143, 2
Bodenheimer, P., & Pollack, J. B. 1986, Icar, 67, 391
Borucki, W. J., Koch, D. G., Basri, G., et al. 2011, ApJ, 736, 19
Carter, J. A., Agol, E., Chaplin, W. J., et al. 2012, Sci, 337, 556
Chiang, E., & Laughlin, G. 2013, MNRAS, 431, 3444
Cochran, W. D., Fabrycky, D. C., Torres, G., et al. 2011, ApJS, 197, 7
Dragomir, D., Matthews, J. M., Eastman, J. D., et al. 2013, ApJL, 772, L2
Dumusque, X., Bonomo, A. S., Haywood, R. D., et al. 2014, ApJ, 789, 154
Elkins-Tanton, L. T., & Seager, S. 2008, ApJ, 685, 1237
Fortney, J. J., Marley, M. S., & Barnes, J. W. 2007, ApJ, 659, 1661
Fortney, J. J., Mordasini, C., Nettelmann, N., et al. 2013, ApJ, 775, 80
Fressin, F., Torres, G., Charbonneau, D., et al. 2013, ApJ, 766, 81
Gillon, M., Demory, B.-O., Benneke, B., et al. 2012, A&A, 539, A28
Guillot, T., Chabrier, G., Gautier, D., & Morel, P. 1995, ApJ, 450, 463
Hansen, B. M. S., & Murray, N. 2013, ApJ, 775, 53
Hatzes, A. P., Fridlund, M., Nachmani, G., et al. 2011, ApJ, 743, 75
Hayashi, C., Nakazawa, K., & Nakagawa, Y. 1985, in Protostars and Planets II, ed. D. C. Black & M. S. Matthews (Tucson, AZ: Univ. Arizona Press), 1100
Henning, W. G., O'Connell, R. J., & Sasselov, D. D. 2009, ApJ, 707, 1000
Howard, A. W., Marcy, G. W., Bryson, S. T., et al. 2012, ApJS, 201, 15
Howard, A. W., Sanchis-Ojeda, R., Marcy, G. W., et al. 2013, Natur, 503, 381

Hubbard, W. B., Fortney, J. J., Lunine, J. I., et al. 2001, ApJ, 560, 413
Hubbard, W. B., Hattori, M. F., Burrows, A., & Hubeny, I. 2007, ApJL, 658, L59
Ikoma, M., & Hori, Y. 2012, ApJ, 753, 66
Jackson, A. P., Davis, T. A., & Wheatley, P. J. 2012, MNRAS, 422, 2024
Jackson, B., Miller, N., Barnes, R., et al. 2010, MNRAS, 407, 910
Jontof-Hutter, D., Lissauer, J. J., Rowe, J. F., & Fabrycky, D. C. 2014, ApJ, 785, 15
Lecavelier Des Etangs, A. 2007, A&A, 461, 1185
Léger, A., Rouan, D., Schneider, J., et al. 2009, A&A, 506, 287
Lissauer, J. J., Fabrycky, D. C., Ford, E. B., et al. 2011, Natur, 470, 53
Lissauer, J. J., Jontof-Hutter, D., Rowe, J. F., et al. 2013, ApJ, 770, 131
Lopez, E. D., & Fortney, J. J. 2013, ApJ, 776, 2
Lopez, E. D., Fortney, J. J., & Miller, N. 2012, ApJ, 761, 59
Lyon, S. P., & Johnson, J. D. 1992, LANL Rep. LA-UR-92-3407 (Los Alamos: LANL)
Marcus, R. A., Sasselov, D., Hernquist, L., & Stewart, S. T. 2010, ApJL, 712, L73
Marcus, R. A., Stewart, S. T., Sasselov, D., & Hernquist, L. 2009, ApJL, 700, L118
Marley, M. S., Fortney, J. J., Hubickyj, O., Bodenheimer, P., & Lissauer, J. J. 2007, ApJ, 655, 541
Miller, N., & Fortney, J. J. 2011, ApJL, 736, L29
Mordasini, C. 2013, A&A, 558, A113
Mordasini, C., Alibert, Y., Georgy, C., et al. 2012, A&A, 547, A112
Morley, C. V., Fortney, J. J., Kempton, E. M.-R., et al. 2013, ApJ, 775, 33
Morton, T. D., & Swift, J. J. 2013, arXiv:1303.3013
Nettelmann, N., Fortney, J. J., Kramm, U., & Redmer, R. 2011, ApJ, 733, 2
Nettelmann, N., Holst, B., Kietzmann, A., et al. 2008, ApJ, 683, 1217
Owen, J. E., & Jackson, A. P. 2012, MNRAS, 425, 2931
Owen, J. E., & Wu, Y. 2013, ApJ, 775, 105
Pepe, F., Cameron, A. C., Latham, D. W., et al. 2013, Natur, 503, 377
Petigura, E. A., Howard, A. W., & Marcy, G. W. 2013a, PNAS, 110, 19273
Petigura, E. A., Marcy, G. W., & Howard, A. W. 2013b, ApJ, 770, 69
Queloz, D., Bouchy, F., Moutou, C., et al. 2009, A&A, 506, 303
Ribas, I., Guinan, E. F., Güdel, M., & Audard, M. 2005, ApJ, 622, 680
Rogers, L. A., Bodenheimer, P., Lissauer, J. J., & Seager, S. 2011, ApJ, 738, 59
Rogers, L. A., & Seager, S. 2010a, ApJ, 712, 974
Rogers, L. A., & Seager, S. 2010b, ApJ, 716, 1208
Saumon, D., Chabrier, G., & van Horn, H. M. 1995, ApJS, 99, 713
Thompson, S. L. 1990, ANEOS—Analytic Equations of State for Shock Physics Codes, Sandia Natl. Lab. Doc. SAND89-2951
Valencia, D., Guillot, T., Parmentier, V., & Freedman, R. S. 2013, ApJ, 775, 10
Valencia, D., Ikoma, M., Guillot, T., & Nettelmann, N. 2010, A&A, 516, A20
Valencia, D., Sasselov, D. D., & O'Connell, R. J. 2007, ApJ, 665, 1413
Weiss, L. M., Marcy, G. W., Rowe, J. F., et al. 2013, ApJ, 768, 14
Wright, J. T., Fakhouri, O., Marcy, G. W., et al. 2011, PASP, 123, 412
Xie, J. W., Wu, Y., & Lithwick, Y. 2014, ApJ, 789, 165
Zahnle, K. J., & Catling, D. C. 2013, Lunar and Planetary Institute Science Conference Abstracts, Vol. 44, Lunar and Planetary Institute Science Conference Abstracts, 2787
Zapolsky, H. S., & Salpeter, E. E. 1969, ApJ, 158, 809